

Optimizing superconductivity: from cuprates via nickelates to palladates

Motoharu Kitatani^{a,b}, Liang Si^{c,d}, Paul Worm^d, Jan M. Tomczak^{d,e}, Ryotaro Arita^{b,f} and Karsten Held^d

^aDepartment of Material Science, University of Hyogo, Ako, Hyogo 678-1297, Japan

^bRIKEN Center for Emergent Matter Sciences (CEMS), Wako, Saitama, 351-0198, Japan

^cSchool of Physics, Northwest University, Xi'an 710127, China

^dInstitute of Solid State Physics, TU Wien, 1040 Vienna, Austria

^eDepartment of Physics, King's College London,
Strand, London WC2R 2LS, United Kingdom and

^fResearch Center for Advanced Science and Technology,
University of Tokyo 4-6-1, Komaba, Meguro-ku, Tokyo 153-8904, Japan

(Dated: June 13, 2023)

Motivated by cuprate and nickelate superconductors, we perform a comprehensive study of the superconducting instability in the single-band Hubbard model. We calculate the spectrum and superconducting transition temperature T_c as a function of filling and Coulomb interaction for a range of hopping parameters, using the dynamical vertex approximation. We find the sweet spot for high T_c to be at intermediate coupling, moderate Fermi surface warping, and low hole doping. Combining these results with first principles calculations, neither nickelates nor cuprates are close to this optimum within the single-band description. Instead, we identify some palladates, notably $\text{RbSr}_2\text{PdO}_3$ and $A'_2\text{PdO}_2\text{Cl}_2$ ($A'=\text{Ba}_{0.5}\text{La}_{0.5}$), to be virtually optimal, while others, such as NdPdO_2 , are too weakly correlated.

Introduction—Ever since the discovery of cuprate superconductivity [1], the material dependence of the transition temperature T_c and exploring routes toward optimizing T_c are a central quest of condensed matter physics. The recently discovered nickelate superconductors provide a new perspective to this quest. Similar to cuprates, superconductivity in nickelates emerges from a doped $3d^{9-\delta}$ ($\delta \sim 0.2$) electronic configuration of the transition metal. Besides the initial infinite-layer superconductor $\text{Nd}_{1-x}\text{Sr}_x\text{NiO}_2$ [2–8], substituting neodymium with another lanthanoid [9–11] and also the quintuple-layer compound [12] show superconductivity. This indicates that, akin to cuprates, there is a whole family of nickelate superconductors.

As for the theoretical modeling, the one-band Hubbard model is arguably the simplest effective model for cuprates [13, 14]. Its tight-binding parameters can be obtained from *ab initio* calculations, and the relation between model parameters and the experimental T_c has been analyzed [15–27]. For nickelates, a similar scenario (1) with a one-band Hubbard model plus largely decoupled electron pockets has been put forward [28–35]. Based on the same density functional theory (DFT) and dynamical mean-field theory (DMFT) Fermi surface with Ni $3d_{x^2-y^2}$ orbital plus electron pockets around A and Γ momentum, a second group of scenarios (2) [36–39] emphasizes the role of holes in the Ni $3d_{z^2}$ orbital. These originate from an admixture around the Γ pocket that is predominately Nd $5d_{z^2}$. In scenario (1) this is argued not to be of primary importance for superconductivity because of the strong doping and rare earth cation dependence of the Γ pocket [3, 40–42]. Finally, scenario (3) proposes an *additional* Ni $3d_{z^2}$ Fermi surface based on self-interaction corrected (sic) DFT+DMFT [32, 43–46]. Such an additional Fermi surface is also obtained in an-

tiferromagnetically ordered DFT [47, 48], GW +DMFT [49], and DFT+DMFT in the overdoped region [28, 50].

While the relevant low energy model for nickelates is still under debate, a boost for scenario (1) was its successful prediction of the superconducting phase diagram [28] prior to experiments [5, 6] and with high accuracy in the light of new, defect-free films [51]. Also some other experiments including, among others, the Hall coefficient, resonant x-ray spectroscopy [52] and magneto transport [53] point toward this scenario. As for the microscopic origin of high- T_c superconductivity: while spin fluctuations mediate superconductivity in Ref. [28], the topic remains highly controversial; many different mechanisms have been proposed [54–57].

The aim of the present paper is hence two-fold: First, we would like to identify the optimal conditions for superconductivity in the Hubbard model building upon recent progress made with diagrammatic extensions of DMFT [58]. In particular, we will employ the dynamical vertex approximation (D Γ A) [59], which accurately describes antiferromagnetic spin fluctuations in the parameter range where numerical quantum Monte-Carlo simulations are still available [60]. Second, from a materials point of view we would like to identify cuprate- or nickelate-like materials that promise even higher T_c 's. One important factor is the interaction strength U and its ratio to the hopping U/t . On a qualitative level it has been recently found [28, 61] that the interaction strength is too large in nickelates. Higher T_c 's should thus be possible using compressive strain or pressure [62], confirmed experimentally by a record $T_c > 30$ K for nickelates under a pressure of 12 GPa with no saturation yet discernible [63]. Much more dramatic changes of U/t are possible when going from $3d$ to $4d$ transition metal oxides, which

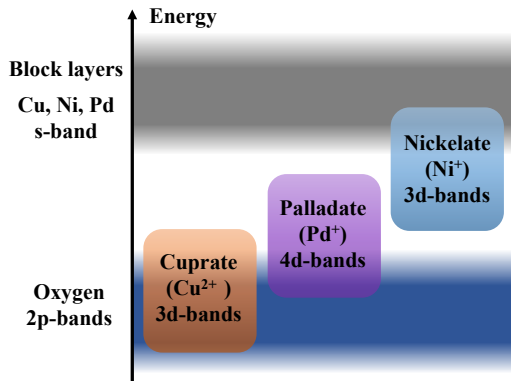


FIG. 1. (Color online) Schematic picture of the energy levels for copper (Cu^{2+}), nickel (Ni^+), palladium (Pd^+) superconductors.

can be achieved by replacing Ni with Pd [28, 33, 64, 65]. Here, we study this possibility on a quantitative level. We show that a one-band description is justified for palladates, and make a prediction of the superconducting phase diagram which can be tested in experiment.

Let us start by sketching the electronic structures of the above-mentioned materials schematically in Fig. 1. As is well known, the parent cuprate compounds are charge transfer insulators [66]; Cu-3d and O-2p bands exist at a similar energy level and are strongly hybridized. Thus the Hubbard model is justified only as an effective model that mimics the physics of the Zhang-Rice singlet [14]. In contrast, the Ni 3d-orbital is higher up in energy by ~ 1 eV. The increased distance to the oxygen orbitals then makes the single- $d_{x^2-y^2}$ -orbital description more suitable than for the CuO_2 layers in cuprates. However, density-functional theory (DFT) calculations [61, 65, 67–72] show that the Ni- d bands of NdNiO_2 now partially overlap instead with the bands of Nd in-between the NiO_2 layers, forming the already mentioned pockets around the A and Γ momentum.

If we replace Ni (3d) with Pd (4d), the Pd 4d-orbitals are shifted back down by ~ 1 eV due to the higher ionization energy of Pd compared to Ni. This removes the pockets present in the nickelates and leads to a larger d - p hybridization and minor overlap with the oxygen bands. However, we do not yet have a charge transfer state as in the cuprates. Indeed, our DFT and DMFT computations (shown in Supplementary Materials (SM) [73] Section I-III) of the crystal and electronic structures of the nickelate NdNiO_2 and the palladates NdPdO_2 , $\text{RbSr}_2\text{PdO}_3$ and $A_2\text{PdO}_2\text{Cl}_2$ show that palladate compounds are somewhere in-between cuprates and nickelates – with a single-band $d_{x^2-y^2}$ Fermi surface justifying a modelling by a single-orbital Hubbard model. Tuning the dispersion and interaction strength in palladates thus opens so-far untapped possibilities for finding new superconductors with possibly higher T_c 's.

	$ t $ (meV)	t'/t	t''/t	U_{eff}/t
NdNiO_2	395	-0.25	0.12	8
NdNiO_2 (Strained)	419	-0.23	0.12	7.0–7.5
NdPdO_2	558	-0.17	0.13	4.5
$\text{RbSr}_2\text{PdO}_3$	495	-0.24	0.16	6
$A_2\text{PdO}_2\text{Cl}_2$	443	-0.22	0.14	7.5
$A_2\text{PdO}_2\text{Cl}_2$ (-1.5% strain)	470	-0.22	0.14	7.0
$A_2\text{PdO}_2\text{Cl}_2$ (-3.0% strain)	497	-0.22	0.14	6.0

TABLE I. Summary of the DFT-derived parameters for the single-band Hubbard model, as an effective low-energy model for the nickelate NdNiO_2 , the palladates NdPdO_2 , $\text{RbSr}_2\text{PdO}_3$, and $A_2\text{PdO}_2\text{Cl}_2$.

Model and Method—We study the two-dimensional Hubbard model on the square lattice with Hamiltonian

$$\mathcal{H} = \sum_{\mathbf{k}, \sigma} \epsilon_{\mathbf{k}} c_{\mathbf{k}, \sigma}^\dagger c_{\mathbf{k}, \sigma} + U \sum_i n_{i, \uparrow} n_{i, \downarrow}, \quad (1)$$

where $c_{\mathbf{k}, \sigma}^\dagger$ ($c_{\mathbf{k}, \sigma}$) is the creation (annihilation) operator,

$$\epsilon_{\mathbf{k}} = -2t[\cos(k_x) + \cos(k_y)] - 4t' \cos(k_x) \cos(k_y) - 2t''[\cos(2k_x) + \cos(2k_y)], \quad (2)$$

the energy-momentum dispersion, U the onsite Coulomb repulsion, and t, t', t'' are the nearest, second nearest, and third nearest hoppings, respectively. The model parameters are obtained from DFT, using WIEN2K [74] with the PBE [75, 76] exchange correlation functional and WIEN2WANNIER [77] for projecting onto a maximally localized $3d_{x^2-y^2}$ Wannier orbital [78]. SM Sec. VI, VII, VIII, and IX provides details on the Wannier projection, the DFT calculation of $A_2\text{PdO}_2\text{Cl}_2$, the stability against structural distortions, and the antiferromagnetic DFT solution, respectively. Before constructing the single-orbital model for palladates, we performed multi-orbital DMFT calculations which confirm the single orbital nature of the system, see SM [73] Sec. III. The constrained random phase approximation (cRPA) is employed to estimate U . Following the previous research [28], we employed slightly enhanced values (+0.35 eV [79]) from our cRPA calculation for entangled bands [80]: 2.85 eV for NdNiO_2 , 2.55 eV for $\text{RbSr}_2\text{PdO}_2$, and 2.97 eV for $A_2\text{PdO}_2\text{Cl}_2$ (which are consistent with the preceding study [65]; please note that small changes in the interaction strength U do not change our conclusion). Table I provides a summary of the DFT and cRPA derived parameters [81] (for details see SM [73] Section II), which are used in subsequent DGA calculations. Besides these material-specific Hubbard models we also include the simplest case with nearest-neighbor hopping only ($t' = t'' = 0$).

We analyze these single-orbital models by means of the DGA [59, 82–84], a diagrammatic extension of DMFT [85–87]. Similar techniques have been previously applied

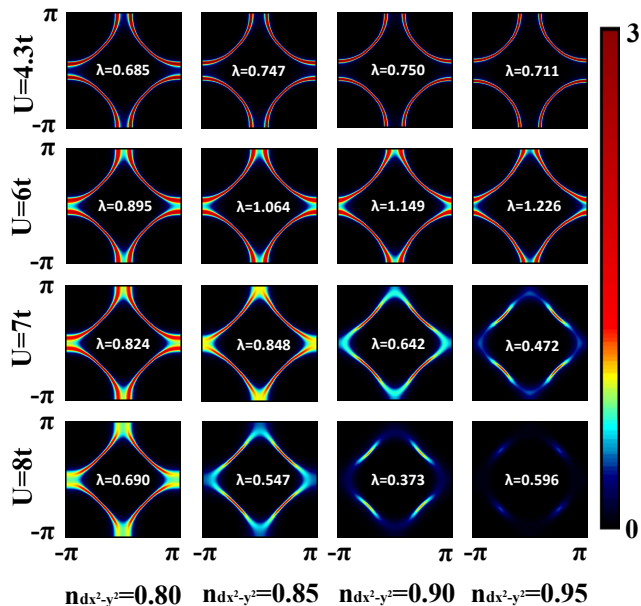


FIG. 2. (Color online) DFA Spectrum (momentum dependence of the imaginary part of the Green function $-\Im G/\pi$ at lowest Matsubara frequency) for different interactions ($U/t = 4.3, 6.0, 7.0, 8.0$) and fillings ($n = 0.80, 0.85, 0.90, 0.95$) at $T = 0.01t, t'/t = -0.17, t''/t = 0.13$. Corresponding d -wave superconductivity eigenvalues λ are also shown.

to unconventional superconductivity on the square lattice [88–95]. We mainly use the continuous-time quantum Monte-Carlo solver from w2dynamics[96] as DMFT solver, see SM [73] for details. DFA simultaneously includes strong correlations and long-range spatial (charge and spin) fluctuations. Both are essential for modelling superconductivity in correlated electron systems. Most importantly, DFA can describe dynamical screening effects which are crucial for accurately determining T_c [97]. It has predicted the superconducting dome in nickelates [28] prior to experiments [5, 6, 51] with astonishing accuracy. For a review of DFA, see [58]; and [98] for how to calculate T_c .

Spectrum—We first discuss the electronic spectrum. In Fig. 2, we show the momentum dependence of the imaginary part of the Green’s function at the lowest Matsubara frequency: $-\Im G(\omega_n = \pi/\beta, \mathbf{k})/\pi$ for various interactions: $U/t = 4.3, 6, 7, 8$ and fillings: $n = 0.80, 0.85, 0.90, 0.95$ for hoppings corresponding to NdPdO₂ ($t'/t = -0.17, t''/t = 0.13$). We observe that the spectrum changes from a non-interacting-like Fermi surface at weak coupling to a shape with strongly momentum-dependent damping at stronger coupling, before, finally, all spectral weight is removed. In between, we obtained a Fermi arc structure at low doping ($n_{d_{x^2-y^2}} \sim 0.90 - 0.95$) for $U = 7t$ and $8t$, which is a hallmark feature of cuprates.

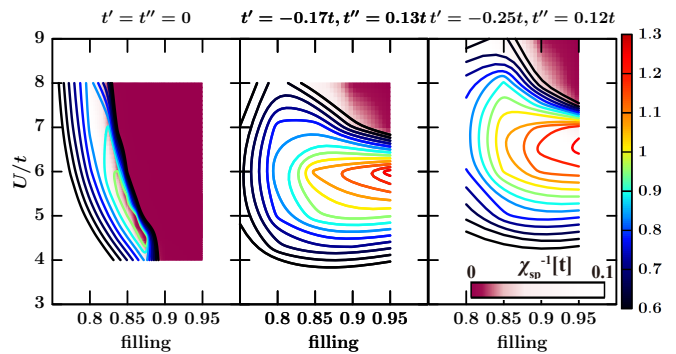


FIG. 3. (Color online) Superconducting eigenvalue λ and antiferromagnetic susceptibility $\chi_{\text{sp}}(Q_{\text{max}}, \omega = 0)$ as a function of interaction U and filling at $T = 0.01t$ for the three different t', t'' given at the top of each panel.

Even outside the pseudogap region, correlation effects change the Fermi surface structure. Specifically, they decrease the Fermi surface warping, i.e. effectively decrease t' . Such change of the spectrum for large (t', t'') region has also been observed in other theoretical studies [99–101]. These Fermi surface changes also affect the superconducting instability. While this effect (coming from the momentum dependence of $\Re \Sigma$) is minor compared with the pseudogap physics (stemming from the momentum dependence of $\Im \Sigma$), we find that such a Fermi surface flattening can enhance superconductivity, but only around the optimal conditions in parameter space; see SM [73] for a detailed discussion.

As demonstrated here, DFA properly captures correlation induced changes of the Fermi surface (e.g., Fermi arc in cuprates [102]) and is consistent with previous results. *Superconductivity*—Next, we discuss the superconducting instability. To do so, we calculate the eigenvalues of the linearized gap (Eliashberg) equation which is the usual procedure for evaluating the superconducting instability from the paramagnetic solution. The eigenvalue λ is a measure of the superconducting instability, and T_c is identified by λ reaching unity. While DFA is unbiased with respect to spin, charge and quantum critical fluctuations, we find that spin fluctuations mediate d -wave superconductivity in all cases studied.

In Fig. 3, we plot the superconducting eigenvalues against the interaction U and the filling for three tight-binding parameter sets: the simplest case ($t' = t'' = 0$), parameters for NdPdO₂ ($t' = -0.17t, t'' = 0.13t$) and NdNiO₂ ($t' = -0.25t, t'' = 0.12t$). First, we notice in all cases a strong suppression of λ around half-filling at strong coupling. This leads to a dome structure of T_c as a function of both interaction strength and filling, which is essential for optimizing superconducting materials.

Fig. 3 unequivocally reveals that the origin of this suppression is too strong antiferromagnetic correlations (dark red color scale). These open a pseudogap in Fig. 2 and thus suppress the electron propagator. Even though

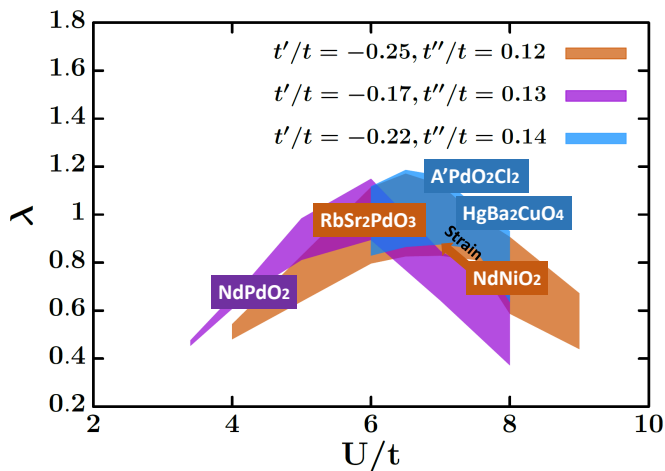


FIG. 4. (Color online) Interaction U dependence of the superconducting eigenvalues λ at $T = 0.01t$ for three different t', t'' from Table I. For each U , the linewidth corresponds to the range of λ for fillings $0.80 \leq n \leq 0.90$. Materials corresponding to these models and U 's are indicated.

the antiferromagnetic pairing glue is huge, this eventually suppresses superconductivity.

Let us note that cluster DMFT [103] shows a similar tendency as in Fig. 3, albeit with still much higher temperatures and weaker superconducting fluctuations. The pseudogap behavior is, on the other hand, consistent with the observation that the insulating regime expands if long-range spatial fluctuations are properly included [60, 104, 105].

Except for the perfectly nested case ($t' = t'' = 0$) where spin-fluctuations are overly strong and open a gap regardless of interaction strength, we can separate the U -range into two regions: For weak couplings ($U \lesssim 5$), there is only a weak doping dependence. For strong coupling ($U \gtrsim 7$), on the other hand, a pronounced filling dependence develops, with antiferromagnetic fluctuation dominating around half-filling and suppressing λ . Optimal conditions for superconductivity in the one-band 2D square-lattice Hubbard model are realized in between these two regions. The importance of the finite Fermi surface warping was also suggested in early phenomenological material-dependence studies of cuprate superconductors [15]. The only other possibilities to significantly enhance T_c are (i) increasing t , which sets the energy scale, while keeping all parameter ratios constant, or (ii) creating a positive feedback on superconductivity from other bands including the oxygen bands in case of cuprates [17, 106, 107].

Fig. 4 demonstrates that a dome shape of λ develops as a function of U . The optimal U slightly depends on the (t', t'') parameters. This trend can be explained by the earlier onset of the pseudogap for systems with small t', t'' , due to better (antiferromagnetic) nesting.

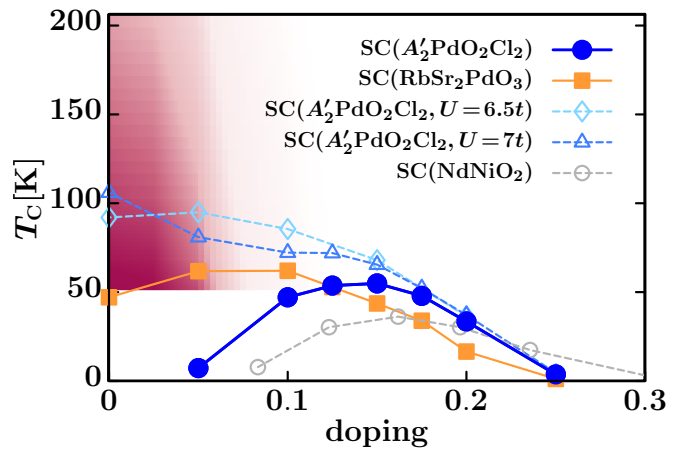


FIG. 5. (Color online) Phase diagrams for nickelates (NdNiO_2) and palladates ($\text{RbSr}_2\text{PdO}_3$ and $\text{A}'_2\text{PdO}_2\text{Cl}_2$). In the red region, we expect antiferromagnetism instead of superconductivity for $\text{A}'_2\text{PdO}_2\text{Cl}_2$ if there is a weak inter-layer coupling because of the huge χ_{sp} (color code of χ_{sp} in DGA as in Fig. 3).

In Fig. 4, we also show the points corresponding to each material from Table I. Further we include $\text{HgBa}_2\text{CuO}_4$ as a typical cuprate which has $U/t \sim 7.5t - 8t$ [22, 24, 25] and almost the same t', t'' as $\text{A}'_2\text{PdO}_2\text{Cl}_2$. As mentioned in previous works [28, 61], we can see that NdNiO_2 has a too large interaction and thus falls outside the area with highest T_c .

Following this insight, we can rationalize now the recent experimental achievements of realizing higher T_c 's in NdNiO_2 : both external pressure [63] and in-plane lattice compressive strains [51, 108] play similar roles at reducing the in-plane lattice constant, shrinking the Ni-Ni distance and weakening the correlation strength U/t , while increasing the magnetic exchange $4t^2/U$ [109]. Simply replacing Ni-3d by Pd-4d yields NdPdO_2 which is too weakly correlated in Fig. 4. Let us emphasize that this concerns tetragonal NdPdO_2 which can be stabilized in thin films. In the bulk and for thick films, there will be a substantial orthorhombic distortion, see SM [73] Section VIII. Due to the tilting of the PdO_6 octahedra, t is reduced to 304 meV. This pushes orthorhombic NdPdO_2 to $U/t \sim 7$, i.e., close to the optimum in Fig. 4 (average $t'/t \approx -0.25$; $t''/t \approx 0$). However this enhancement of T_c/t is largely compensated by the smaller t , altogether yielding a similar T_c .

A more promising solution to increase U/t and thus T_c is to enlarge the lattice which is possible by inserting spacing layers between the PdO_2 planes. Doing so, our DFT and cRPA calculations indeed place $\text{RbSr}_2\text{PdO}_3$ and $\text{A}'_2\text{PdO}_2\text{Cl}_2$ close to the optimum.

We finally show in Fig. 5 the phase diagram for these palladate compounds, using the same approach as previously for nickelates [28]. We predict palladates to

have a $T_c \gtrsim 60$ K, which touches the floor level line of cuprates and remarkably exceeds the current upper limit of nickelates, $T_c = 30$ K [51, 63]. Indeed, the calculated phase diagram (superconductivity and antiferromagnetism) for $A_2PdO_2Cl_2$ is quite similar to well-known cuprate phase diagrams. Furthermore, weak strain (described by $U = 6.5t, 7t$ [110], c.f., Table I) would tune the material to an even higher T_c .

Conclusion and outlook—Building on the success of DGA to predict the superconducting dome in nickelates, we have performed a comprehensive survey of the Hubbard model and revealed the optimal phase-space region for unconventional superconductivity. Conditions are optimal at intermediate coupling ($U/t = 6 - 7$), moderate Fermi surface warping ($|t'| + |t''| \approx 0.3 - 0.4$), and low hole doping ($n \sim 0.90 - 0.95$). Combining this insight with first principles calculations, we predict palladates and nickelates grown on compressive substrates to be superconductors with a T_c comparable to cuprates.

The theoretically proposed palladates have yet to be synthesized. Palladates with a perovskite-like structure [111, 112], however, have already been realized in experiment. Then, provided that a reduction process, similar to that of $NdNiO_3 \rightarrow NdNiO_2$, is possible, realizing palladates with PdO_2 layers is a promising route for high- T_c superconductors. Additionally, the possibility to engineer cuprate analogs based on $4d$ materials has been discussed based on AgF_2 [113] and silver oxides [114]. Analyzing the relation between those systems and the ones we are proposing in this letter will offer fresh insight into the design of superconductors.

Acknowledgments—We would like to thank Motoaki Hirayama and Yusuke Nomura for illuminating discussions. We thank Alaska Subedi for providing us with lower symmetry phase structures of nickelates from Ref. 115. We acknowledge the financial support by Grant-in-Aids for Scientific Research (JSPS KAKENHI) Grant No. JP21K13887 and JP19H05825 as well as by projects P32044 and I5398 of the Austrian Science Funds (FWF). Calculations have been done mainly on the Vienna Scientific Cluster (VSC).

[1] J. G. Bednorz and K. A. Müller, *Zeitschrift für Physik B Condensed Matter* **64**, 189 (1986).
 [2] D. Li, K. Lee, B. Y. Wang, M. Osada, S. Crossley, H. R. Lee, Y. Cui, Y. Hikita, and H. Y. Hwang, *Nature* **572**, 624 (2019).
 [3] L. Si, W. Xiao, J. Kaufmann, J. M. Tomczak, Y. Lu, Z. Zhong, and K. Held, *Phys. Rev. Lett.* **124**, 166402 (2020).
 [4] P. Werner and S. Hoshino, *Phys. Rev. B* **101**, 041104 (2020).
 [5] S. Zeng, C. S. Tang, X. Yin, C. Li, M. Li, Z. Huang, J. Hu, W. Liu, G. J. Omar, H. Jani, Z. S. Lim, K. Han, D. Wan, P. Yang, S. J. Pennycook, A. T. S. Wee, and

A. Ariando, *Phys. Rev. Lett.* **125**, 147003 (2020).
 [6] D. Li, B. Y. Wang, K. Lee, S. P. Harvey, M. Osada, B. H. Goodge, L. F. Kourkoutis, and H. Y. Hwang, *Phys. Rev. Lett.* **125**, 027001 (2020).
 [7] M. Hepting, D. Li, C. J. Jia, H. Lu, E. Paris, Y. Tseng, X. Feng, M. Osada, E. Been, Y. Hikita, and et al., *Nature Materials* (2020), 10.1038/s41563-019-0585-z.
 [8] Y. Nomura and R. Arita, *Reports on Progress in Physics* **85**, 052501 (2022).
 [9] M. Osada, B. Y. Wang, K. Lee, D. Li, and H. Y. Hwang, *Phys. Rev. Materials* **4**, 121801 (2020).
 [10] S. Zeng, C. Li, L. E. Chow, Y. Cao, Z. Zhang, C. S. Tang, X. Yin, Z. S. Lim, J. Hu, P. Yang, and A. Ariando, *Science Advances* **8**, eabl9927 (2022).
 [11] M. Osada, B. Y. Wang, B. H. Goodge, S. P. Harvey, K. Lee, D. Li, L. F. Kourkoutis, and H. Y. Hwang, *Advanced Materials* **33**, 2104083 (2021).
 [12] G. A. Pan, D. F. Segedin, H. LaBollita, Q. Song, E. M. Nica, B. H. Goodge, A. T. Pierce, S. Doyle, S. Novakov, D. C. Carrizales, A. T. N'Diaye, P. Shafer, H. Paik, J. T. Heron, J. A. Mason, A. Yacoby, L. F. Kourkoutis, O. Erten, C. M. Brooks, A. S. Botana, and J. A. Mundy, *Nature Materials* **21**, 160 (2022).
 [13] P. W. Anderson, *Science* **235**, 1196 (1987).
 [14] F. C. Zhang and T. M. Rice, *Phys. Rev. B* **37**, 3759 (1988).
 [15] E. Pavarini, I. Dasgupta, T. Saha-Dasgupta, O. Jepsen, and O. K. Andersen, *Phys. Rev. Lett.* **87**, 047003 (2001).
 [16] H. Sakakibara, H. Usui, K. Kuroki, R. Arita, and H. Aoki, *Phys. Rev. Lett.* **105**, 057003 (2010).
 [17] C. Weber, C. Yee, K. Haule, and G. Kotliar, *EPL (Europhysics Letters)* **100**, 37001 (2012).
 [18] H. Sakakibara, K. Suzuki, H. Usui, S. Miyao, I. Maruyama, K. Kusakabe, R. Arita, H. Aoki, and K. Kuroki, *Phys. Rev. B* **89**, 224505 (2014).
 [19] S. W. Jang, H. Sakakibara, H. Kino, T. Kotani, K. Kuroki, and M. J. Han, *Scientific reports* **6**, 33397 (2016).
 [20] S. Teranishi, K. Nishiguchi, and K. Kusakabe, *Journal of the Physical Society of Japan* **87**, 114701 (2018).
 [21] M. Hirayama, Y. Yamaji, T. Misawa, and M. Imada, *Phys. Rev. B* **98**, 134501 (2018).
 [22] F. Nilsson, K. Karlsson, and F. Aryasetiawan, *Phys. Rev. B* **99**, 075135 (2019).
 [23] H. Sakakibara and T. Kotani, *Phys. Rev. B* **99**, 195141 (2019).
 [24] M. Hirayama, T. Misawa, T. Ohgoe, Y. Yamaji, and M. Imada, *Phys. Rev. B* **99**, 245155 (2019).
 [25] S. Teranishi, K. Nishiguchi, and K. Kusakabe, *Journal of the Physical Society of Japan* **90**, 054705 (2021).
 [26] H. Watanabe, T. Shirakawa, K. Seki, H. Sakakibara, T. Kotani, H. Ikeda, and S. Yunoki, *Phys. Rev. Research* **3**, 033157 (2021).
 [27] J.-B. Morée, M. Hirayama, M. T. Schmid, Y. Yamaji, and M. Imada, *Phys. Rev. B* **106**, 235150 (2022).
 [28] M. Kitatani, L. Si, O. Janson, R. Arita, Z. Zhong, and K. Held, *npj Quantum Materials* **5**, 59 (2020).
 [29] J. Karp, A. S. Botana, M. R. Norman, H. Park, M. Zingl, and A. Millis, *Phys. Rev. X* **10**, 021061 (2020).
 [30] P. Worm, L. Si, M. Kitatani, R. Arita, J. M. Tomczak, and K. Held, *Phys. Rev. Materials* **6**, L091801 (2022).
 [31] T. Y. Xie, Z. Liu, C. Cao, Z. F. Wang, J. L. Yang, and W. Zhu, *Phys. Rev. B* **106**, 035111 (2022).

- [32] H. Chen, A. Hampel, J. Karp, F. Lechermann, and A. J. Millis, *Frontiers in Physics* **10** (2022), 10.3389/fphy.2022.835942.
- [33] K. Held, L. Si, P. Worm, O. Janson, R. Arita, Z. Zhong, J. M. Tomczak, and M. Kitatani, *Frontiers in Physics* **9** (2022), 10.3389/fphy.2021.810394.
- [34] J. Karp, A. Hampel, and A. J. Millis, *Phys. Rev. B* **105**, 205131 (2022).
- [35] C. Lane, R. Zhang, B. Barbiellini, R. S. Markiewicz, A. Bansil, J. Sun, and J.-X. Zhu, arXiv preprint arXiv:2208.08375 (2022).
- [36] K.-W. Lee and W. E. Pickett, *Phys. Rev. B* **70**, 165109 (2004).
- [37] P. Adhikary, S. Bandyopadhyay, T. Das, I. Dasgupta, and T. Saha-Dasgupta, *Phys. Rev. B* **102**, 100501 (2020).
- [38] Y. Wang, C.-J. Kang, H. Miao, and G. Kotliar, *Phys. Rev. B* **102**, 161118 (2020).
- [39] Z. Wang, G.-M. Zhang, Y.-f. Yang, and F.-C. Zhang, *Phys. Rev. B* **102**, 220501 (2020).
- [40] I. Leonov, S. L. Skornyakov, and S. Y. Savrasov, *Phys. Rev. B* **101**, 241108 (2020).
- [41] S. Ryee, H. Yoon, T. J. Kim, M. Y. Jeong, and M. J. Han, *Phys. Rev. B* **101**, 064513 (2020).
- [42] E. Been, W.-S. Lee, H. Y. Hwang, Y. Cui, J. Zaanen, T. Devereaux, B. Moritz, and C. Jia, *Phys. Rev. X* **11**, 011050 (2021).
- [43] F. Lechermann, *Phys. Rev. B* **101**, 081110 (2020).
- [44] F. Lechermann, *Phys. Rev. X* **10**, 041002 (2020).
- [45] A. Kreisel, B. M. Andersen, A. T. Römer, I. M. Eremin, and F. Lechermann, *Phys. Rev. Lett.* **129**, 077002 (2022).
- [46] F. Lechermann, *Phys. Rev. B* **105**, 155109 (2022).
- [47] X. Wan, V. Ivanov, G. Resta, I. Leonov, and S. Y. Savrasov, *Phys. Rev. B* **103**, 075123 (2021).
- [48] M.-Y. Choi, W. E. Pickett, and K.-W. Lee, *Phys. Rev. Research* **2**, 033445 (2020).
- [49] F. Petocchi, V. Christiansson, F. Nilsson, F. Aryasetiawan, and P. Werner, *Phys. Rev. X* **10**, 041047 (2020).
- [50] The rather crude classification [(1) $3d_{x^2-y^2}$ plus decoupled pockets; (2) same Fermi surface as (1) but relevance of $3d_{z^2}$ holes and coupling to the pockets; (3) additional $3d_{z^2}$ Fermi surface, possibly no pockets] neglects finer details, e.g., Hund's vs. Kondo physics in (2) or the conjectured importance of $4f$ electrons [116, 117].
- [51] K. Lee, B. Y. Wang, M. Osada, B. H. Goodge, T. C. Wang, Y. Lee, S. Harvey, W. J. Kim, Y. Yu, C. Murthy, S. Raghu, L. F. Kourkoutis, and H. Y. Hwang, arXiv:2203.02580 (2022).
- [52] K. Higashi, M. Winder, J. Kuneš, and A. Hariki, *Phys. Rev. X* **11**, 041009 (2021).
- [53] W. Sun, Y. Li, R. Liu, J. Yang, J. Li, S. Yan, H. Sun, W. Guo, Z. Gu, Y. Deng, *et al.*, arXiv preprint arXiv:2204.13264 (2022).
- [54] P. A. Lee, N. Nagaosa, and X.-G. Wen, *Rev. Mod. Phys.* **78**, 17 (2006).
- [55] D. J. Scalapino, *Rev. Mod. Phys.* **84**, 1383 (2012).
- [56] E. Fradkin, S. A. Kivelson, and J. M. Tranquada, *Rev. Mod. Phys.* **87**, 457 (2015).
- [57] B. Keimer, S. A. Kivelson, M. R. Norman, S. Uchida, and J. Zaanen, *Nature* **518**, 179 (2015).
- [58] G. Rohringer, H. Hafermann, A. Toschi, A. A. Katanin, A. E. Antipov, M. I. Katsnelson, A. I. Lichtenstein, A. N. Rubtsov, and K. Held, *Rev. Mod. Phys.* **90**, 025003 (2018).
- [59] A. Toschi, A. A. Katanin, and K. Held, *Phys. Rev. B* **75**, 045118 (2007).
- [60] T. Schäfer, N. Wentzell, F. Šimkovic, Y.-Y. He, C. Hille, M. Klett, C. J. Eckhardt, B. Arzhang, V. Harkov, F. m. c.-M. Le Régent, A. Kirsch, Y. Wang, A. J. Kim, E. Kozik, E. A. Stepanov, A. Kauch, S. Andergassen, P. Hansmann, D. Rohe, Y. M. Vil'k, J. P. F. LeBlanc, S. Zhang, A.-M. S. Tremblay, M. Ferrero, O. Parcollet, and A. Georges, *Phys. Rev. X* **11**, 011058 (2021).
- [61] H. Sakakibara, H. Usui, K. Suzuki, T. Kotani, H. Aoki, and K. Kuroki, *Phys. Rev. Lett.* **125**, 077003 (2020).
- [62] L. Si, P. Worm, and K. Held, *Crystals* **12** (2022), 10.3390/cryst12050656.
- [63] N. N. Wang, M. W. Yang, Z. Yang, K. Y. Chen, H. Zhang, Q. H. Zhang, Z. H. Zhu, Y. Uwatoko, L. Gu, X. L. Dong, J. P. Sun, K. J. Jin, and J. G. Cheng, *Nature Communications* **13**, 4367 (2022).
- [64] A. S. Botana and M. R. Norman, *Phys. Rev. Materials* **2**, 104803 (2018).
- [65] M. Hirayama, T. Tadano, Y. Nomura, and R. Arita, *Phys. Rev. B* **101**, 075107 (2020).
- [66] J. Zaanen, G. A. Sawatzky, and J. W. Allen, *Phys. Rev. Lett.* **55**, 418 (1985).
- [67] A. S. Botana and M. R. Norman, *Phys. Rev. X* **10**, 011024 (2020).
- [68] L.-H. Hu and C. Wu, *Phys. Rev. Research* **1**, 032046 (2019).
- [69] X. Wu, D. Di Sante, T. Schwemmer, W. Hanke, H. Y. Hwang, S. Raghu, and R. Thomale, *Phys. Rev. B* **101**, 060504 (2020).
- [70] Y. Nomura, M. Hirayama, T. Tadano, Y. Yoshimoto, K. Nakamura, and R. Arita, *Phys. Rev. B* **100**, 205138 (2019).
- [71] G.-M. Zhang, Y.-f. Yang, and F.-C. Zhang, *Phys. Rev. B* **101**, 020501 (2020).
- [72] M. Jiang, M. Berciu, and G. A. Sawatzky, *Phys. Rev. Lett.* **124**, 207004 (2020).
- [73] Supplemental information regarding details of DFT, DMFT and DFA calculations, as well as spectra, are available at XXX, which includes Ref. [118–139].
- [74] P. Blaha, K. Schwarz, F. Tran, R. Laskowski, G. K. H. Madsen, and L. D. Marks, *The Journal of Chemical Physics* **152**, 074101 (2020).
- [75] J. P. Perdew, K. Burke, and M. Ernzerhof, *Phys. Rev. Lett.* **77**, 3865 (1996).
- [76] J. P. Perdew, A. Ruzsinszky, G. I. Csonka, O. A. Vydrov, G. E. Scuseria, L. A. Constantin, X. Zhou, and K. Burke, *Phys. Rev. Lett.* **100**, 136406 (2008).
- [77] J. Kuneš, R. Arita, P. Wissgott, A. Toschi, H. Ikeda, and K. Held, *Computer Physics Communications* **181**, 1888 (2010).
- [78] N. Marzari, A. A. Mostofi, J. R. Yates, I. Souza, and D. Vanderbilt, *Rev. Mod. Phys.* **84**, 1419 (2012).
- [79] We employed a slightly different version of cRPA calculations [80] than previously [28], to better capture material differences. While we still enhance U to mimic the frequency dependence and other over-screening effects, the enhancement used here is slightly smaller than in Ref. 28.
- [80] T. Miyake, F. Aryasetiawan, and M. Imada, *Phys. Rev. B* **80**, 155134 (2009).
- [81] Single orbital parameters for two palladates: $\text{RbSr}_2\text{PdO}_3$ and $\text{A}_2\text{PdO}_2\text{Cl}_2$ are already derived

- in the preceding study [24]. We obtained consistent results in our calculation and used them for further DMFT and DfA calculations.
- [82] K. Held, A. Katanin, and A. Toschi, *Progress of Theoretical Physics (Supplement)* **176**, 117 (2008).
- [83] A. A. Katanin, A. Toschi, and K. Held, *Phys. Rev. B* **80**, 075104 (2009).
- [84] H. Kusunose, *J. Phys. Soc. Jpn.* **75**, 054713 (2006).
- [85] W. Metzner and D. Vollhardt, *Phys. Rev. Lett.* **62**, 324 (1989).
- [86] A. Georges, G. Kotliar, W. Krauth, and M. J. Rozenberg, *Rev. Mod. Phys.* **68**, 13 (1996).
- [87] G. Kotliar and D. Vollhardt, *Physics Today* **57**, 53 (2004).
- [88] J. Otsuki, H. Hafermann, and A. I. Lichtenstein, *Phys. Rev. B* **90**, 235132 (2014).
- [89] M. Kitatani, N. Tsuji, and H. Aoki, *Phys. Rev. B* **92**, 085104 (2015).
- [90] M. Kitatani, N. Tsuji, and H. Aoki, *Phys. Rev. B* **95**, 075109 (2017).
- [91] J. Vučićević, T. Ayril, and O. Parcollet, *Phys. Rev. B* **96**, 104504 (2017).
- [92] D. Vilardi, C. Taranto, and W. Metzner, *Phys. Rev. B* **99**, 104501 (2019).
- [93] S. Sayyad, E. W. Huang, M. Kitatani, M.-S. Vaezi, Z. Nussinov, A. Vaezi, and H. Aoki, *Phys. Rev. B* **101**, 014501 (2020).
- [94] G. V. Astretsov, G. Rohringer, and A. N. Rubtsov, *Phys. Rev. B* **101**, 075109 (2020).
- [95] M. Kitatani, Y. Nomura, M. Hirayama, and R. Arita, *arXiv preprint arXiv:2205.00239* (2022), [10.48550/arXiv.2205.00239](https://arxiv.org/abs/2205.00239).
- [96] M. Wallerberger, A. Hausoel, P. Gunacker, A. Kowalski, N. Parragh, F. Goth, K. Held, and G. Sangiovanni, *Computer Physics Communications* **235**, 388 (2019).
- [97] M. Kitatani, T. Schäfer, H. Aoki, and K. Held, *Phys. Rev. B* **99**, 041115 (2019).
- [98] M. Kitatani, R. Arita, T. Schäfer, and K. Held, *Journal of Physics: Materials* **5**, 034005 (2022).
- [99] W. Wu, M. S. Scheurer, S. Chatterjee, S. Sachdev, A. Georges, and M. Ferrero, *Phys. Rev. X* **8**, 021048 (2018).
- [100] R. Rossi, F. Šimkovic, and M. Ferrero, *EPL (Europhysics Letters)* **132**, 11001 (2020).
- [101] M. Klett, P. Hansmann, and T. Schäfer, *Frontiers in Physics* **10** (2022), [10.3389/fphy.2022.834682](https://doi.org/10.3389/fphy.2022.834682).
- [102] T. Yoshida, X. J. Zhou, K. Tanaka, W. L. Yang, Z. Husain, Z.-X. Shen, A. Fujimori, S. Sahrakorpi, M. Lindroos, R. S. Markiewicz, A. Bansil, S. Komiya, Y. Ando, H. Eisaki, T. Kakeshita, and S. Uchida, *Phys. Rev. B* **74**, 224510 (2006).
- [103] X. Chen, J. P. F. LeBlanc, and E. Gull, *Phys. Rev. Lett.* **115**, 116402 (2015).
- [104] T. Schäfer, F. Geles, D. Rost, G. Rohringer, E. Arrigoni, K. Held, N. Blümer, M. Aichhorn, and A. Toschi, *Phys. Rev. B* **91**, 125109 (2015).
- [105] F. Šimkovic, J. P. F. LeBlanc, A. J. Kim, Y. Deng, N. V. Prokof'ev, B. V. Svistunov, and E. Kozik, *Phys. Rev. Lett.* **124**, 017003 (2020).
- [106] D. Rybicki, M. Jurkutat, S. Reichardt, C. Kapusta, and J. Haase, *Nature communications* **7**, 11413 (2016).
- [107] N. Kowalski, S. S. Dash, P. Sémon, D. Sénéchal, and A.-M. Tremblay, *Proceedings of the National Academy of Sciences* **118**, e2106476118 (2021), <https://www.pnas.org/doi/pdf/10.1073/pnas.2106476118>.
- [108] X. Ren, Q. Gao, Y. Zhao, H. Luo, X. Zhou, and Z. Zhu, *arXiv preprint arXiv:2109.05761* (2021), [10.48550/arXiv.2109.05761](https://arxiv.org/abs/2109.05761).
- [109] O. Ivashko, M. Horio, W. Wan, N. B. Christensen, D. E. McNally, E. Paris, Y. Tseng, N. E. Shaik, H. M. Rønnow, H. I. Wei, C. Adamo, C. Lichtensteiger, M. Gibert, M. R. Beasley, K. M. Shen, J. M. Tomczak, T. Schmitt, and J. Chang, *Nature Communications* **10**, 786 (2019).
- [110] For drawing the $U = 6.5t$ phase diagram, we averaged the -1.5% , -3.0% -strain result from Table I.
- [111] S.-J. Kim, S. Lemaux, G. Demazeau, J.-Y. Kim, and J.-H. Choy, *Journal of Materials Chemistry* **12**, 995 (2002).
- [112] S.-J. Kim, S. Lemaux, G. Demazeau, J.-Y. Kim, and J.-H. Choy, *Journal of the American Chemical Society* **123**, 10413 (2001).
- [113] J. Gawraczyński, D. Kurzydłowski, R. A. Ewings, S. Bandaru, W. Gadomski, Z. Mazej, G. Ruani, I. Bergenti, T. Jaroń, A. Ozarowski, *et al.*, *Proceedings of the National Academy of Sciences* **116**, 1495 (2019).
- [114] M. Hirayama, M. Thobias Schmid, T. Tadano, T. Misawa, and M. Imada, *arXiv:2207.12595* (2022).
- [115] A. Subedi, *Phys. Rev. Mater.* **7**, 024801 (2023).
- [116] M.-Y. Choi, K.-W. Lee, and W. E. Pickett, *Phys. Rev. B* **101**, 020503 (2020).
- [117] R. Zhang, C. Lane, B. Singh, J. Nokelainen, B. Barbiellini, R. S. Markiewicz, A. Bansil, and J. Sun, *Communications Physics* **4**, 118 (2021).
- [118] L. Bellaiche and D. Vanderbilt, *Phys. Rev. B* **61**, 7877 (2000).
- [119] F. Tran and P. Blaha, *Phys. Rev. Lett.* **102**, 226401 (2009).
- [120] G. H. Wannier, *Phys. Rev.* **52**, 191 (1937).
- [121] N. Marzari and D. Vanderbilt, *Phys. Rev. B* **56**, 12847 (1997).
- [122] I. Souza, N. Marzari, and D. Vanderbilt, *Phys. Rev. B* **65**, 035109 (2001).
- [123] A. A. Mostofi, J. R. Yates, Y.-S. Lee, I. Souza, D. Vanderbilt, and N. Marzari, *Computer physics communications* **178**, 685 (2008).
- [124] V. I. Anisimov, I. V. Solovyev, M. A. Korotin, M. T. Czyżyk, and G. A. Sawatzky, *Phys. Rev. B* **48**, 16929 (1993).
- [125] E. Gull, A. J. Millis, A. I. Lichtenstein, A. N. Rubtsov, M. Troyer, and P. Werner, *Rev. Mod. Phys.* **83**, 349 (2011).
- [126] J. Kaufmann and K. Held, *arXiv:2105.11211* (2021).
- [127] J. E. Gubernatis, M. Jarrell, R. N. Silver, and D. S. Sivia, *Phys. Rev. B* **44**, 6011 (1991).
- [128] A. W. Sandvik, *Phys. Rev. B* **57**, 10287 (1998).
- [129] T. Schäfer, A. A. Katanin, M. Kitatani, A. Toschi, and K. Held, *Phys. Rev. Lett.* **122**, 227201 (2019).
- [130] P. C. Hohenberg, *Phys. Rev.* **158**, 383 (1967).
- [131] N. D. Mermin and H. Wagner, *Phys. Rev. Lett.* **17**, 1133 (1966).
- [132] C. Eckhardt, K. Hummer, and G. Kresse, *Phys. Rev. B* **89**, 165201 (2014).
- [133] <https://www.mail-archive.com/wien@zeus.theochem.tuwien.ac.at/msg11726.html>.
- [134] A. Togo and I. Tanaka, *Scripta Materialia* **108**, 1 (2015).
- [135] G. Kresse and J. Furthmüller, *Computational materials science* **6**, 15 (1996).
- [136] G. Kresse and J. Furthmüller, *Phys. Rev. B* **54**, 11169

- (1996).
- [137] F. Bernardini, A. Bosin, and A. Cano, *Phys. Rev. Materials* **6**, 044807 (2022).
- [138] A. Subedi, arXiv preprint arXiv:2203.11922 (2022).
- [139] C. Xia, J. Wu, Y. Chen, and H. Chen, *Phys. Rev. B* **105**, 115134 (2022).

Supplementary material for “Optimizing superconductivity: from cuprates via nickelates to palladates”

Motoharu Kitatani^{a,b}, Liang Si^{c,d}, Paul Worm^d, Jan M. Tomczak^d, Ryotaro Arita^{b,e} and Karsten Held^d

^aDepartment of Material Science, University of Hyogo, Ako, Hyogo 678-1297, Japan

^bRIKEN Center for Emergent Matter Sciences (CEMS), Wako, Saitama, 351-0198, Japan

^cSchool of Physics, Northwest University, Xi'an 710127, China

^dInstitute of Solid State Physics, TU Wien, 1040 Vienna, Austria and

^eResearch Center for Advanced Science and Technology,

University of Tokyo 4-6-1, Komaba, Meguro-ku, Tokyo 153-8904, Japan

(Dated: June 13, 2023)

This supplementary material contains additional results obtained by density functional theory (DFT), dynamical mean field theory (DMFT) and dynamical vertex approximation (DFA) that further corroborate our conclusions of the main text and is organized in nine sections. In Section I, we perform discussions on the crystal structures, parameters and analyze similarities and differences between the nickelate NdNiO_2 and the palladates NdPdO_2 , $\text{RbSr}_2\text{PdO}_3$ and $A'_2\text{PdO}_2\text{Cl}_2$ ($A' = \text{La}_{0.5}\text{Ba}_{0.5}$). Section II provides detailed DFT (and beyond DFT) results of electronic structure computations for all compounds. In Section III we show the DMFT results, including spectral functions and effective mass, for $\text{RbSr}_2\text{PdO}_3$ and $A'_2\text{PdO}_2\text{Cl}_2$. Section IV shows the self-energy effect on the spectrum and the superconductivity instability in more detail. In Section V, we show the numerical details on the DFA study of superconductivity. Further, in Section VI we present our Wannier function projection and in Section VII the computational details of the virtual crystal approximation. Section VIII analyzes the phonon dispersion and structural distortions of LaPdO_2 . Finally in Section IX we compute the DFT total energy for different magnetic states of $A'_2\text{PdO}_2\text{Cl}_2$.

I. CRYSTAL STRUCTURE OF NICKELATES AND PALLADATES

The crystal structures of nickelate NdNiO_2 and palladates NdPdO_2 , $\text{RbSr}_2\text{PdO}_3$ and $A'_2\text{PdO}_2\text{Cl}_2$ are shown in Fig. S.1. To guarantee a $3d^9$ configuration of the Ni^{1+} cation in $A'_2\text{PdO}_2\text{Cl}_2$, we need a $A'^{2.5+}$ cation which can be achieved by mixing 50%La and 50%Ba. To approach optimal filling/doping in the proposed palladates $\text{RbSr}_2\text{PdO}_3$ and $A'_2\text{PdO}_2\text{Cl}_2$, the ratio between $\text{Rb}^{1+}/\text{Sr}^{2+}$ for the former and $\text{La}^{3+}/\text{Ba}^{2+}$ for the later case can be tuned.

The relaxed parameters for all nickelates and palladates are shown in Table S.I. For the DFT-level calculations, PBESol [1] is employed for structural relaxations, and PBE [2] for electronic structure calculations (e.g., DFT band structures and tight-binding Wannier projections), following the lines of Ref. [3]. Our PBESol structural relaxations yield the lattice constants of NdNiO_2 $a=b=3.864 \text{ \AA}$ and $c=3.243 \text{ \AA}$. To simulate in-plane compressive strain effects, we tune the in-plane lattices to 3.800 \AA [of bulk LaAlO_3 (LAO)], the z -lattice is then simultaneously relaxed to 3.330 \AA . assuming that the films are several layers thick as in experiments for nickelate superconductors, this change of the lattice parameters is the dominant effect of the substrate; apart from that a bulk DFT calculation is justified. The corresponding changes of hoppings and U are shown in Table I of the main text.

For NdPdO_2 , an in-plane lattice expansion from 3.864 \AA to 4.085 \AA results from substituting Ni by Pd. Such an expansion may contribute to smaller orbital

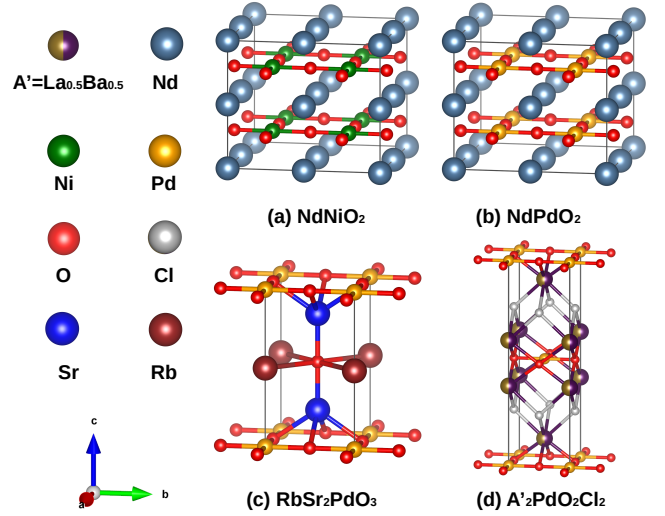


FIG. S.1. Crystal structures of (a) NdNiO_2 , (b) NdPdO_2 , (c) $\text{RbSr}_2\text{PdO}_3$ and (d) $A'_2\text{PdO}_2\text{Cl}_2$.

overlap and stronger electronic correlations if the B -site atoms are unchanged, however the more delocalized $4d$ -orbitals of Pd counteract this with their larger orbital spreads (see main text). When the in-plane lattices are fixed to the one of SrTiO_3 to simulate the strain effects from a STO substrate, the out-of-plane is relaxed to 3.255 \AA , which boosts its two-dimensional characters.

For the proposed palladates $\text{RbSr}_2\text{PdO}_3$ and $A'_2\text{PdO}_2\text{Cl}_2$, the in-plane lattice constants are even larger than those of NdPdO_2 . Another notable difference is the distance between Ni-Ni or Pd-Pd along the

TABLE S.I. DFT-PBESol relaxed lattice parameters of NdNiO₂, NdPdO₂ (with full relaxation or grown on SrTiO₃ substrate), RbSr₂PdO₃ and A₂PdO₂Cl₂ (in units of Å). A' is La_{0.5}Ba_{0.5}. In the last column we show the appropriate substrates, in the brackets are the in-plane lattice constants (also in unit of Å).

-	a/b	c	Ni-Ni/Pd-Pd (in-plane)	out-of-plane	Substrate
NdNiO ₂	3.864	3.243	3.864	3.243	LSAT (3.868)
NdNiO ₂ (strained: on LaAlO ₃)	3.800	3.330	3.800	3.330	LaAlO ₃ (3.80)
NdPdO ₂	4.085	3.143	4.085	3.143	PrScO ₃ (4.02)
NdPdO ₂ (strained: on SrTiO ₃)	3.905	3.255	3.905	3.255	SrTiO ₃ (3.905)
RbSr ₂ PdO ₃	4.264	7.555	4.264	7.555	MgO (4.20)
A ₂ PdO ₂ Cl ₂ (unstrained)	4.366	14.639	4.366	7.944	Rutile-TiO ₂ (4.59)/MgO(4.20)
A ₂ PdO ₂ Cl ₂ (-1.5% strain)	4.301	14.740	4.301	7.973	MgO (4.20)
A ₂ PdO ₂ Cl ₂ (-3% strain)	4.235	14.870	4.235	8.016	MgO (4.20)

z -direction (out-of-plane); it increases to ~ 7.5 - 8.0 Å, as shown in Table S.I. In the last column we list some suitable substrates for the proposed materials, e.g., for RbSr₂PdO₃ and strained (-1.5% and 3%) A₂PdO₂Cl₂ that host larger in-plane lattice constants than SrTiO₃ (3.905 Å), MgO is considerable to be employed as substrate as its in-plane lattice is ~ 4.2 Å. For the fully relaxed NdPdO₂ (4.085 Å), PrScO₃ (in-plane lattice 4.02 Å) is possible candidate. For compressive cases (when compared with the in-plane lattice of SrTiO₃: 3.905 Å) such as unstrained NdNiO₂ and strained NdNiO₂, one of the possible substrates (LaAlO₃)_{0.3}(SrAl_{0.5}Ta_{0.5}O₃)_{0.7} (LSAT: 3.868 Å) had been proved as helpful to enhance its T_c [4]. For the strained case, LaAlO₃ (3.80 Å) is expected to be more effective at eliminating atomic defects and enhancing T_c . The in-plane lattice constant of unstrained A₂PdO₂Cl₂ is predicted as 4.366 Å in DFT structural relaxation, we hence proposed rutile-TiO₂ (4.59 Å) and MgO (4.20 Å) as a possible substrate in realistic experiments.

II. ELECTRONIC STRUCTURE OF NICKELATES AND PALLADATES

To investigate the difference between nickelates and palladates, we first compute their band centroids. The bands centroids in Table S.II are computed by $E_i = \int g_i(E)E dE / \int g_i(E)$, here g_i is the partial density of states of the corresponding orbital i and E is the energy. The integration ranges covers both the bonding and anti-bonding states for Cu/Ni/Pd- d orbital and O- p orbitals (up to 5, 7 and 7 eV for CaCuO₂, NdNiO₂ and NdPdO₂, respectively). As one can see, for the cuprate CaCuO₂, both the centroids of Cu- d and $d_{x^2-y^2}$ are just ~ 0.4 eV and ~ 0.7 eV higher than that of O- p . This is consistent with the fact that CaCuO₂ is a charge-transfer insulator.

For NdNiO₂, the d -bands ($d_{x^2-y^2}$ band) shift up by ~ 1 eV (~ 0.9 eV) compared with those in CaCuO₂. Moreover, the O- p bands are shifted down by ~ 0.9 eV. As a

consequence, the charge transfer energies $\Delta(d-p)$ and $\Delta(d_{x^2-y^2}-p)$ in NdNiO₂ are ~ 1.8 eV larger than in CaCuO₂.

For the palladate NdPdO₂, the band centroid of d -orbitals $E(d)$ is comparable with those of CaCuO₂ while $E(d_{x^2-y^2})$ is ~ 0.3 eV higher than in CaCuO₂. Thus, the charge transfer energies $\Delta(d-p)$ and $\Delta(d_{x^2-y^2}-p)$ are 1.211 and 1.827 eV, i.e., in between the charge transfer energies of CaCuO₂ and NdNiO₂. The computations strongly hint that NdPdO₂ hosts a similar 2D nature as in both CaCuO₂ and NdNiO₂.

In Fig. S.2 we show the DFT-level band structures of NdPdO₂ and RbSr₂PdO₃ and A₂PdO₂Cl₂. NdPdO₂ has a larger $d_{x^2-y^2}$ bandwidth than NdNiO₂, which is due to its more delocalized $4d$ orbitals nature. Its pockets at Γ and A are energetically deeper than in NdNiO₂. However, as concluded by previous research [5], these pockets are not essential for emergent nickelate superconductivity. Additionally, the band structures of A₂PdO₂Cl₂ [Fig. S.2(d)] exhibits a Fermi structure with only the Pd- $d_{x^2-y^2}$ orbital. For RbSr₂PdO₃ [Fig. S.2(c)], the pockets merely touch the Fermi energy at the A and Γ momentum. Indeed, the tiny Γ pocket for RbSr₂PdO₃ is expected to become unoccupied upon hole doping or with exchange-correlations by using functional beyond standard DFT-PBE: the Γ -pocket is absent, e.g., for Rb_{1.2}Sr_{1.8}PdO₃ [Fig. S.3(a)] and RbSr₂PdO₃ computed by employing the improved version of the modified Becke-Johnson (mBJ) exchange potential [Fig. S.3(b)]. On a technical note, the process of hole doping and consequently the noninteger filling at Pd- $d_{x^2-y^2}$ in RbSr₂PdO₃ is achieved here by employing virtual crystal approximation [6].

In Fig. S.3, the band structures of NdPdO₂ [Fig. S.3(d)] on a SrTiO₃ substrate, RbSr₂PdO₃ upon 0.2 hole doping per Pb (i.e., Rb_{1.2}Sr_{1.8}PdO₃) [Fig. S.3(a)], and the bands calculated by improved version of the modified Becke-Johnson exchange potential [7] [Fig. S.3(b)] are shown; for a comparison further the band of fully relaxed NdPdO₂ are presented in Fig. S.3(c). As shown in

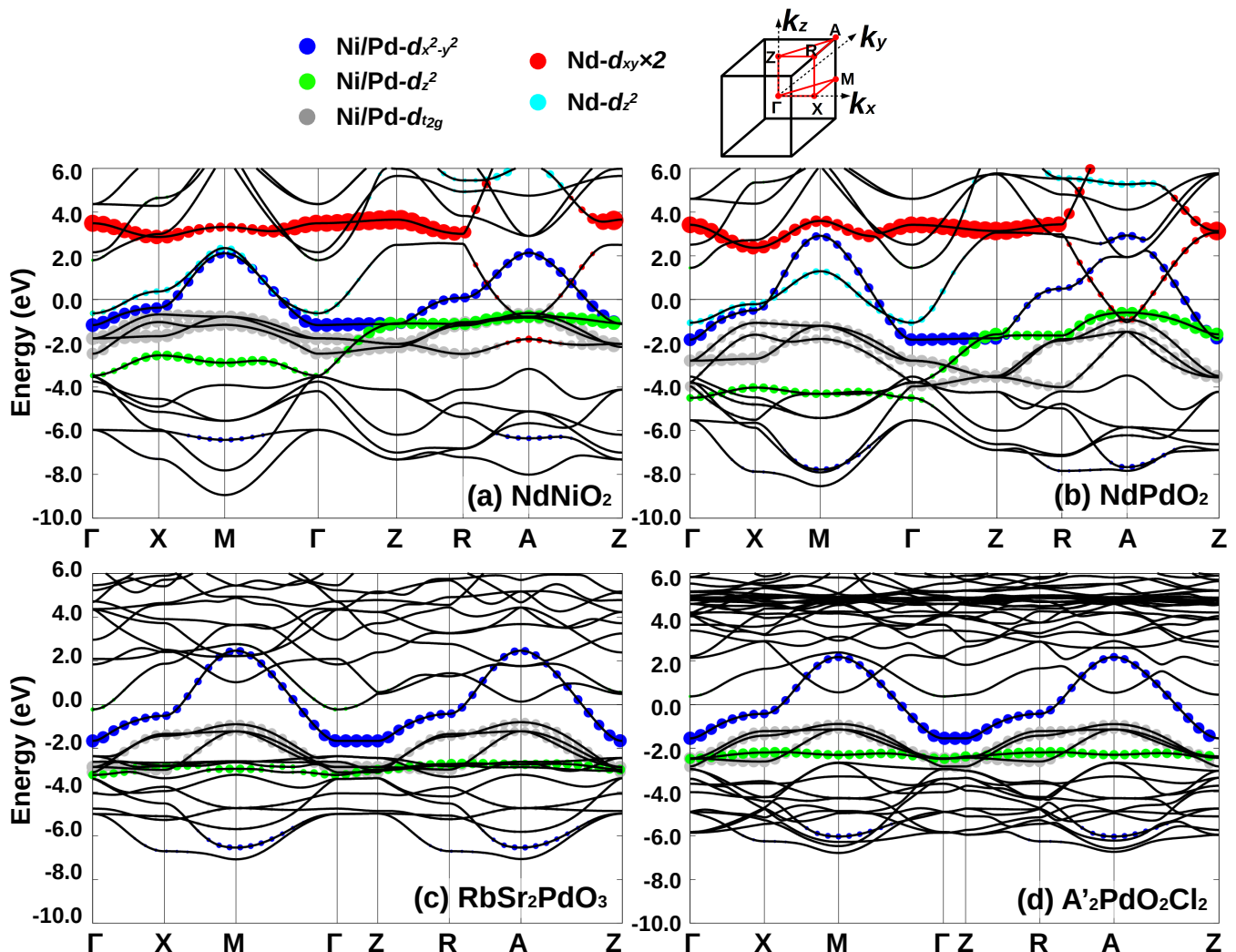


FIG. S.2. DFT band characters of (a) NdNiO₂, (b) NdPdO₂, (c) RbSr₂PdO₃ and (d) A'₂PdO₂Cl₂. Here, we used the fully relaxed structure for all systems. The top panel shows the symbols for different orbitals and the first Brillouin zone. The size of the symbols for Nd- d_{xy} are renormalized by a factor of 2 for clearness.

Fig. S.3(a-b), both hole doping and exchange-correlation potentials are shift the Γ pocket of RbSr₂PdO₃ above the Fermi energy E_f . These results demonstrate that the realistic Fermi surface of RbSr₂PdO₃ can also be expected to be composed of a single band with $d_{x^2-y^2}$ character, even without additional hole doping. The correlations from Pd-4d and the exchange effects, which are both only rudimentarily accounted for in DFT, play an effective role at preserving a 2D cuprates-like Fermi surface.

As we discussed in the main text, the fully relaxed in-plane lattice constants of NdPdO₂ are $a=b=4.085$ Å, 4.6% more than a SrTiO₃ substrate: 3.905 Å. A suitable substrate for an almost unstrained film is PrScO₃ whose lattice is 4.02 Å (as shown in Table S.I). If NdPdO₂ is grown on SrTiO₃, the in-plane lattice is fixed as 3.905 Å. As a consequence, the out-of-plane lattice is relaxed to larger value of 3.255 Å, and thus a better 2D character

TABLE S.II. DFT calculated band centeroids (in units of eV) of CaCuO₂, NdNiO₂ and NdPdO₂ and charge transfer energies Δ .

-	$E(d)$	$E(d_{x^2-y^2})$	$E(O-p)$	$\Delta(d-p)$	$\Delta(d_{x^2-y^2}-p)$
CaCuO ₂	-2.367	-2.047	-2.772	0.405	0.725
NdNiO ₂	-1.384	-1.148	-3.674	2.289	2.525
NdPdO ₂	-2.358	-1.742	-3.570	1.211	1.827

of the $d_{x^2-y^2}$ orbital. As shown in [Fig. S.3(c-d)], such a strain does not change the main character of the Pd- $d_{x^2-y^2}$ orbital.

Finally, as Pd is heavier than Ni, one may consider the spin-orbital coupling (SOC) effects in palladates. We hence perform DFT+SOC band computations for NdPdO₂ (fully relaxed case) with and without SOC, as

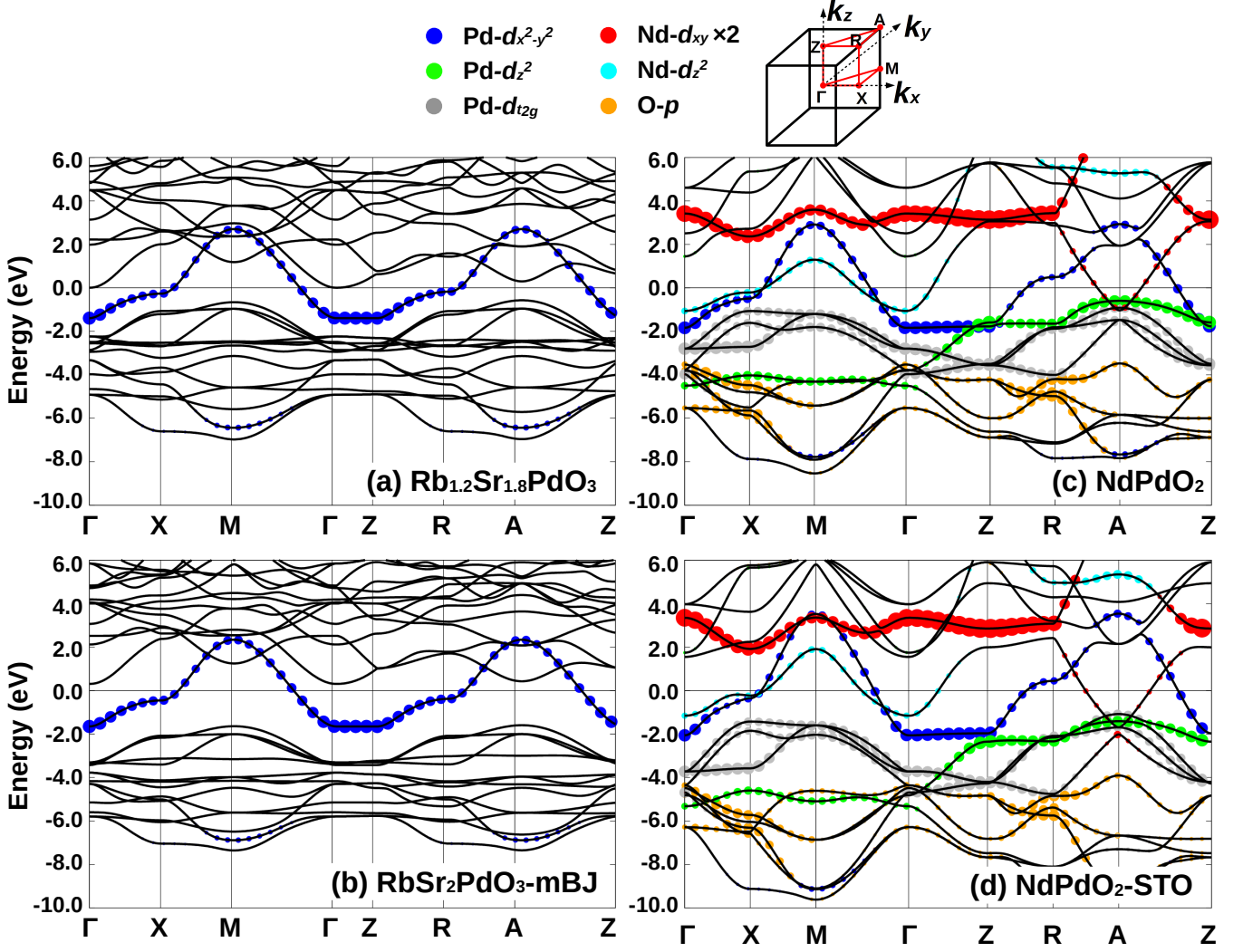


FIG. S.3. Comparison between the DFT band characters of (a) hole doped $\text{Rb}_{1.2}\text{Sr}_{1.8}\text{PdO}_3$, (b) $\text{RbSr}_2\text{PdO}_3$ with mBJ exchange-correlation functional, (c) fully relaxed NdPdO_2 and (d) NdPdO_2 on SrTiO_3 (STO) substrate. The top panel shows the symbols for contribution of the different orbitals and the first Brillouin zone. The size of the symbols for $\text{Nd-}d_{xy}$ are renormalized by a factor of 2 for clarity.

shown in Fig. S.4. Fig. S.4(a) and (b) show the DFT band of NdPdO_2 without and with SOC, respectively. For better visibility, we also plot these bands in a smaller energy region from -2 to 4 eV in Fig. S.4 (c,d). We find three band-crossing regions in which hybridization gaps open after switching-on SOC effect, see S.4(c). The first region is at $E \sim -1$ to -2 eV and $k=X-M$. Here, the SOC opens a hybridization gap between the $\text{Pd-}t_{2g}$ bands. The second region is at $E \sim -0.5$ eV and $k=A$, where there is a band-crossing between $\text{Nd-}d_{xy}$ orbitals, which mostly contribute to the A -pocket, and $\text{Pd-}t_{2g}$ bands. Since these two regions are irrelevant to our target $\text{Pd-}d_{x^2-y^2}$ band, the effect on superconductivity will be minor. The third region is at $E \sim 2$ eV and $k=A$. In Fig. S.4(c), as one see that there is a double-band degeneracy composed of $\text{Nd-}d_{yz}$ and d_{xz} bands, labeled by the arrow in

(c). This double degeneracy exchanges its band characters with $\text{Pd-}d_{x^2-y^2}$ band at A -point. And the gap opens after including SOC effect because the double degeneracy between $\text{Nd-}d_{yz}$ and $\text{Nd-}d_{xz}$ is lost, as shown in the orange region in Fig. S.4(d). However, we can exclude this small band-opening as a possible factor suppressing superconductivity in palladates because the energy of this gap is high (~ 2 eV) compared to E_f at the very top of the energy region of $\text{Pd-}d_{x^2-y^2}$ band (-2 to 3 eV). Additionally, hole-doping will further reduce E_f and weaken this hybridization.

All in all, we conclude that for the low energy physics around the Fermi level, the SOC does not play an important role. This is because there is only a single $\text{Pd-}d_{x^2-y^2}$ band crossing the Fermi level. While SOC could be disadvantageous for superconductivity, in principle,

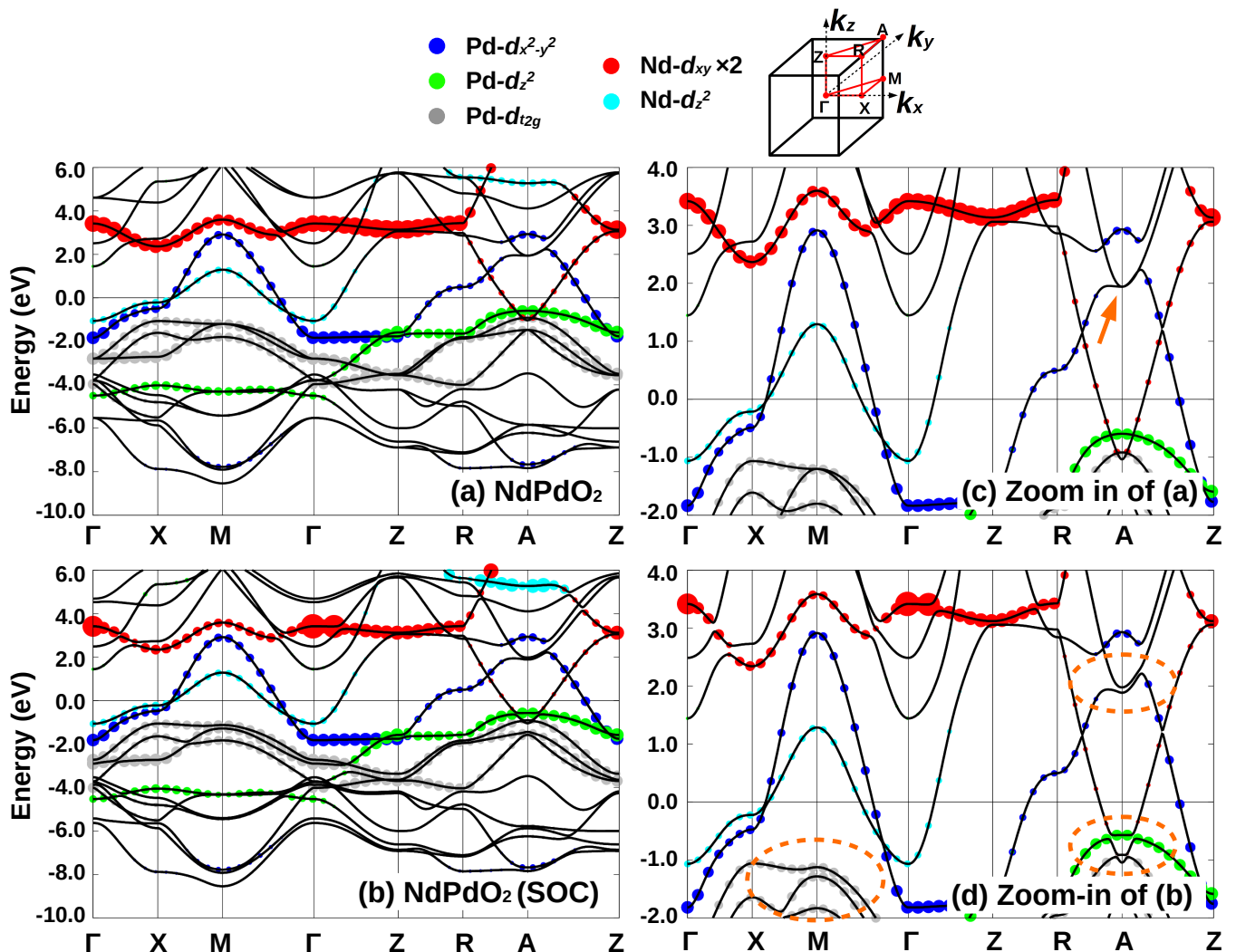


FIG. S.4. Comparison between the DFT band characters of NdPdO_2 with (a,c) and without (b,d) SOC. The arrow in (c) indicates the double degeneracy of the $\text{Nd-}d_{yz}$ and $\text{Nd-}d_{xz}$ orbital at the A point. The dashed orange regions in (d) indicate the SOC induced hybridization gaps.

for superconductivity in the studied palladates it does not seem to be relevant. Hence, we do not consider it in the subsequent DMFT and DGA calculations.

III. FULL d -SHELL PROJECTION IN DMFT

The DFT bands are projected onto maximally localized Wannier functions [8–11] of (i) only the Pd $d_{x^2-y^2}$ band (for the single-band DMFT and DGA calculations presented in the main text) and of (ii) all Pd d bands (for the full- d set calculations in this section), using the WANNIER90 [12] and WIEN2WANNIER [13] codes. These corresponding low-energy effective tight-binding Hamiltonians are generated and subsequently supplemented by a local Kanamori interaction, using the fully localized limit as double counting [14]. DMFT calculations in

the present research are carried out at 300 K with the W2DYNAMICS code [15], which solves the corresponding impurity problem using the continuous time quantum Monte Carlo (CTQMC) approach in the hybridization expansion (CT-HYB) [16]. Real-frequency spectra are obtained with the ANA_CONT code [17] via analytic continuation using the maximum entropy method (MaxEnt) [18, 19].

The corresponding DMFT results of $\text{RdSr}_2\text{PdO}_3$ and $A'_2\text{PdO}_2\text{Cl}_2$ are shown in Fig. S.5, Fig. S.6 and Fig. S.7. Fig. S.5 shows the DMFT k -resolved ($A(k, \omega)$) and k -integrated spectral function ($A(\omega)$) spectral functions of the parent compounds $\text{RdSr}_2\text{PdO}_3$ [Fig. S.5(a)] and $A'_2\text{PdO}_2\text{Cl}_2$ [Fig. S.5(b)], i.e., at $4d^9$ Pd electronic configuration which corresponds to a half-filled $\text{Pd-}d_{x^2-y^2}$ orbital. Including DMFT electronic correlations, the other d -bands ($t_{2g}+d_{z^2}$) of Pd are well separated from

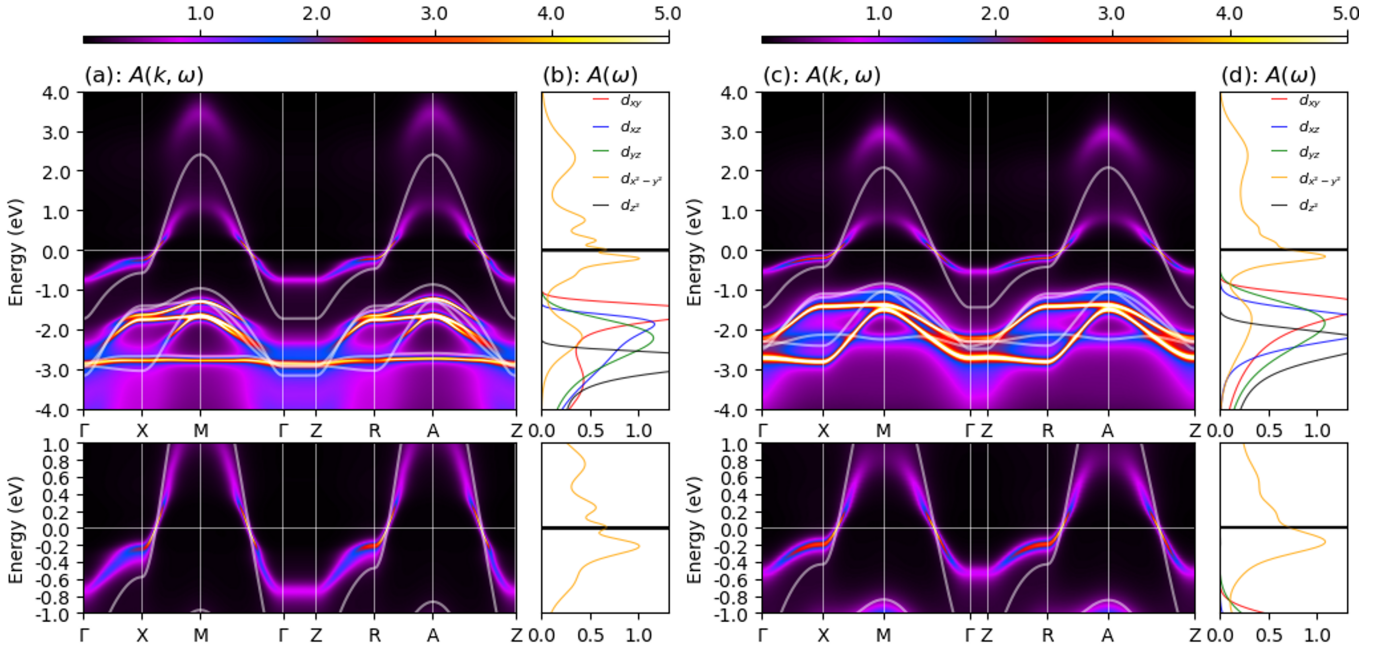


FIG. S.5. Spectral function, k -resolved ($A(k, \omega)$) and k -integrated ($A(\omega)$), for a full d -shell projection at a nominal filling of $n = 9.0$. (Left) $\text{RdSr}_2\text{PdO}_3$ and (right) $\text{A}_2\text{PdO}_2\text{Cl}_2$.

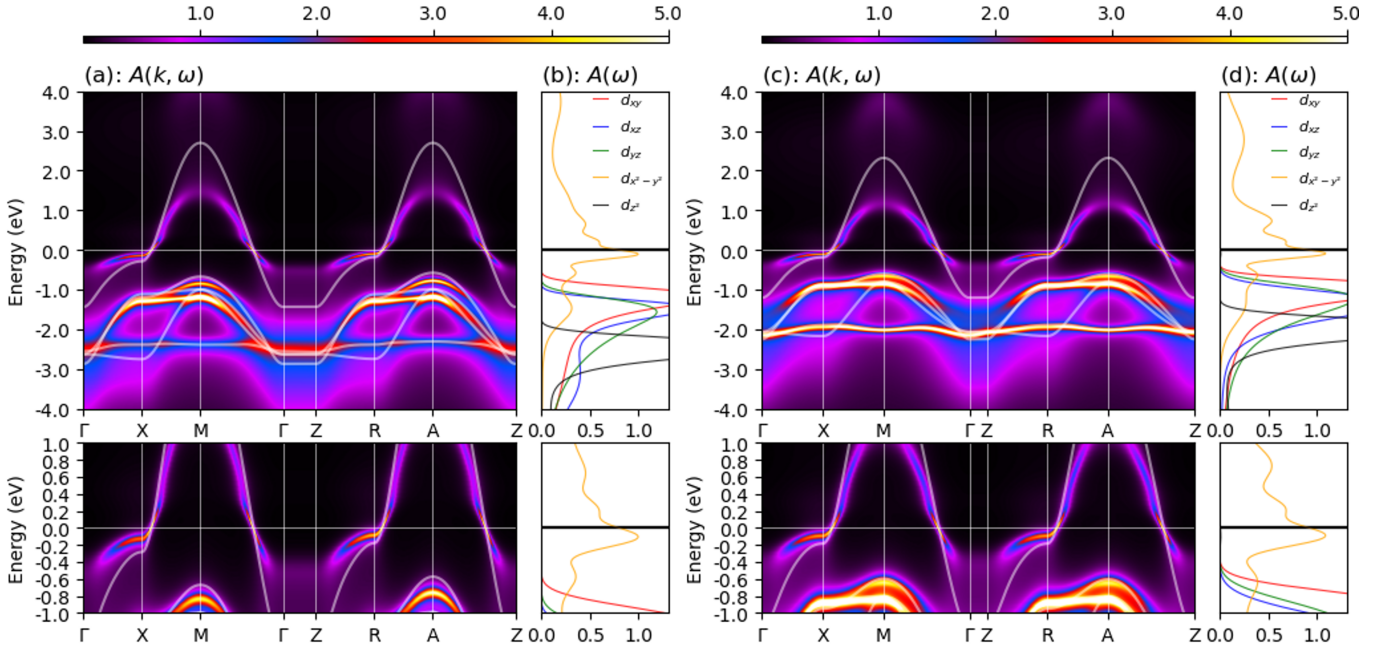


FIG. S.6. Same as Fig. S.5 but now at a nominal filling of $n = 8.8$, which corresponds to the superconducting region.

the $d_{x^2-y^2}$ band. This makes both $\text{RdSr}_2\text{PdO}_3$ and $\text{A}_2\text{PdO}_2\text{Cl}_2$ electronically similar to cuprates superconductors.

Large hole doping had been proved being able to destroy the single-band picture and suppress superconductivity states in both cuprates and nickelates. Hence

it is worth to investigate the electronic structures of $\text{RdSr}_2\text{PdO}_3$ and $\text{A}_2\text{PdO}_2\text{Cl}_2$ with a certain amount of hole doping, in particular, in the hole doping region where superconductivity may be expected. Here, we show the DMFT spectra of $\text{Rd}_{1.2}\text{Sr}_{1.8}\text{PdO}_3$ ($4d^{8.8}$) and

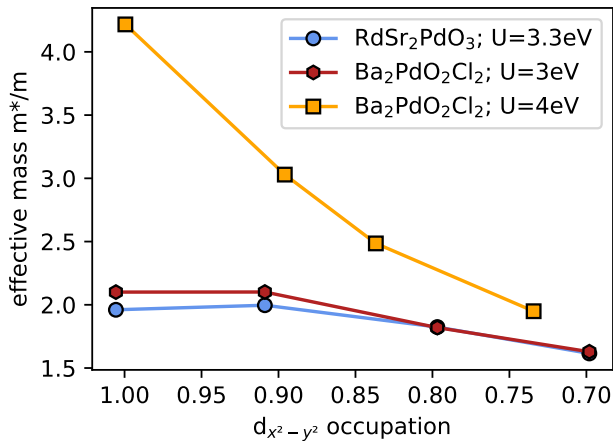


FIG. S.7. Effective mass (m^*/m) as a function of $d_{x^2-y^2}$ occupation for $\text{RdSr}_2\text{PdO}_3$ at $U = 3.3\text{eV}$ (blue) and $\text{Ba}_2\text{PdO}_2\text{Cl}_2$ at $U = 3\text{eV}$ (red) and $U = 4\text{eV}$ (orange).

$A'_2\text{PdO}_2\text{Cl}_2$ (with $A'^{2.4+}=(\text{La}_{0.4}\text{Ba}_{0.6})^{2.4+}$ and consequently $4d^{8.8}$). For both compounds, the single-band $d_{x^2-y^2}$ Fermi surface is conserved.

Finally, we investigate the effective mass (m^*) of both compounds. Fig. S.7 displays the mass renormalization of the $d_{x^2-y^2}$ band as obtained in DMFT (including all Pd d orbitals). For the $A'_2\text{PdO}_2\text{Cl}_2$ compound we show two values of the interaction strength: $U=3.3\text{eV}$ for $\text{RdSr}_2\text{PdO}_3$, 3.3eV and 4eV for $A'_2\text{PdO}_2\text{Cl}_2$. As antiferromagnetic correlations become large towards half-filling so does the effective mass, in particular for the larger interaction. This indicates the strong tendency toward an anti-ferromagnetic Mott insulator at strong coupling. The mass renormalization for both $\text{RdSr}_2\text{PdO}_3$ and $A'_2\text{PdO}_2\text{Cl}_2$ at optimal filling for superconductivity, i.e. $n \sim 1 - 0.8$, is around $m^*/m \sim 2$, which is consistent with the values of NdNiO_2 as n approaches ~ 0.82 per Ni - $d_{x^2-y^2}$: $m^*/m = 2.81$. This comparison indicates that these palladates are quite strongly correlated but less so than NdNiO_2 . This is advantageous for superconductivity, as discussed in the main text.

IV. EFFECT OF FERMI SURFACE SHAPE ON T_c

As shown in the main text, the self-energy weakens the spectral intensity and flattens the Fermi surface shape. Here, we discuss these effects on the Fermi surface structure in more detail, by artificially separating the different effects.

In Fig. S.8, we show the spectrum at two interaction strength [(a) $U = 7.5t$ and (b) $U = 6.5t$] comparing the full DGA and DMFT self-energy [top left (DGA) and top right subpanels (DMFT) in (a) and (b)] to the following artificially modified DGA self-energies: only the real part

[$\text{Im}\Sigma = 0$; middle left subpanels], only the imaginary part [$\text{Re}\Sigma = 0$; bottom left subpanels], momentum averaged DGA self-energy [Σ_{ave} , middle right subpanels] and momentum average for the real part only, keeping the momentum-dependence of the imaginary part [$\text{Re}\Sigma_{\text{ave}}$, bottom right subpanels]. We fix the filling to the original value (i.e., recalculate the chemical potential) for all cases. We also show the corresponding superconductivity eigenvalues λ calculated with these spectra, while keeping the pairing vertex the same for solving the linearized gap equation.

We can first see that the imaginary part of the self-energy has the most relevant effect; it leads to the pseudogap physics, as expected: From DGA to $\text{Im}\Sigma = 0$ in Fig. S.8, the shape of the Fermi surface remains the same, but its intensity becomes stronger, in particular in the antinodal region around $(\pi, 0)$. The corresponding superconducting eigenvalues is a factor 6-7 higher. This clearly shows that the pseudogap is counterproductive for superconductivity.

Comparing DGA to $\text{Im}\Sigma = 0$ and the non-interacting Fermi surface (white dots in the top left subpanels) further shows that the flattening of the Fermi surface is still captured for $\text{Im}\Sigma = 0$. That is it is caused by the real part of the DGA self-energy, hence there is also no flattening in the $\text{Re}\Sigma = 0$ Fermi surface.

Next, if we compare the DMFT self-energy and the momentum averaged DGA self-energy, they give similar results. That is, the Fermi surface structure is similar to the non-interaction line (white dots in top left subpanels). Some self-energy damping exists in both cases, but as a matter of course, there is no momentum differentiation and hence no pseudogap. In this case, the superconductivity eigenvalues are in between those for $\text{Im}\Sigma = 0$ and the DGA self-energy.

When ignoring the momentum dependence of the real part of the self-energy, $\text{Re}\Sigma = 0$ and $\text{Re}\Sigma_{\text{k-ave}}$ give similar results in Fig. S.8. The Fermi surface is the same as in the non-interacting case, but strong damping exists around the anti-nodal $(\pi, 0)$ region (and symmetrically related momenta). This is a consequence of the momentum differentiation of the imaginary part of the DGA self-energy.

When we focus on the effect of the Fermi surface flattening on superconductivity, we can compare the superconducting eigenvalue λ for $\text{Re}\Sigma = 0$ and $\text{Re}\Sigma_{\text{k-ave}}$ with the original DGA λ . We surprisingly find the flattening of the Fermi surface suppresses superconductivity at $U = 7.5t, t' = -0.22t, t'' = 0.14t, n = 0.85$ but enhances it at $U = 6.5t, t' = -0.25t, t'' = 0.12t, n = 0.95$.

To study this dichotomy further, We analyze the parameter dependence in Fig. S.9. We can see that there is almost no effect of $\text{Re}\Sigma$ in the weak coupling regime. In contrast, at strong coupling, the eigenvalues are almost everywhere suppressed if the flattening of the Fermi surface is properly included in Fig. S.9 (a). This Fermi

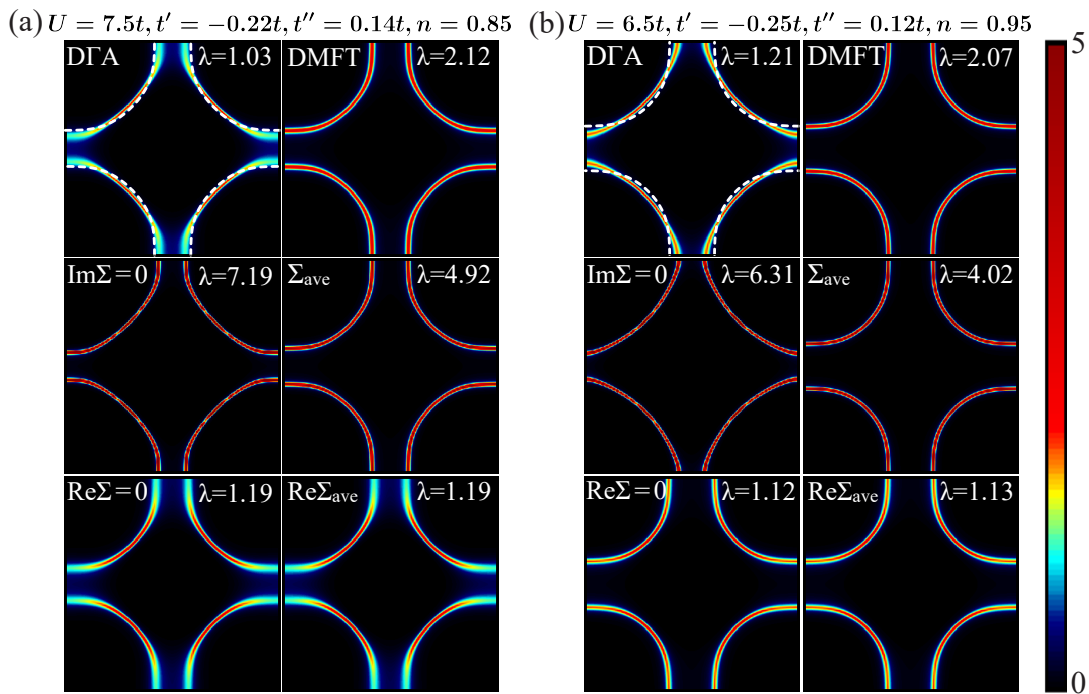


FIG. S.8. Spectrum and superconductivity eigenvalues with DMFT, DΓA and artificially modified self-energies (see text) at $\beta t = 100$ for $U = 7.5t, t' = -0.22t, t'' = 0.14t, n = 0.85$ (left) and $U = 6.5t, t' = -0.25t, t'' = 0.12t, n = 0.95$ (right).

surface flattening, given by the real part of the DΓA self-energy, enhances T_c only around the optimum in the original phase diagram in Fig. S.9(a). That is, for intermediate U and fillings closer to half filling.

This result can be understood as follows: If the strength of the spectrum is similar, i.e., if there is no pseudogap, spectral weight closer to $(\pi, 0)$ is favorable because the (d -wave) gap function has a peak there and because the van Hove singularity results in a particular strong spectral contribution. On the other hand, if the pseudogap opens around $(\pi, 0)$, this trend will eventually reverse. For weak coupling, the Fermi surface flattening does not occur nor does the pseudogap open. There is hence no effect. For larger interactions, the flattening of the Fermi surface moves the Fermi surface toward $(\pi, 0)$. At intermediate coupling, there is no pseudogap yet [see Fig. S.8 (b)] and superconductivity becomes enhanced. This leads to the optimum (or hot spot) for superconductivity in Fig. S.9 (a) at $U \approx 6t$ and $n \approx 0.95$. In contrast for larger interactions a pseudogap opens [see Fig. S.8 (a)]. Thus despite the flattened Fermi surface, superconductivity is suppressed. If it was possible to switch of this pseudogap [as in the artificial $\text{Im}\Sigma = 0$ panel of Fig. S.8 (a)] we would get the strongest tendency toward superconductivity in this parameter regime.

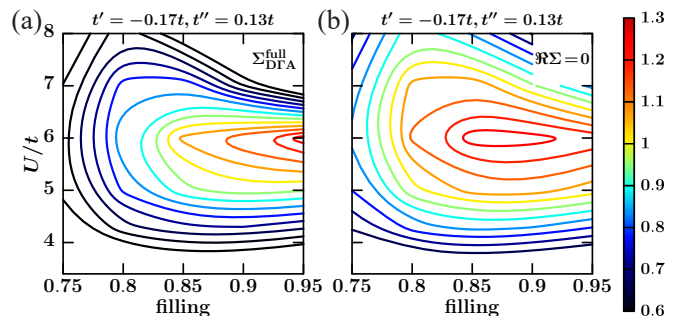


FIG. S.9. Comparison of superconductivity eigenvalues when using the full DΓA self-energy ($\Sigma_{\text{D}\Gamma\text{A}}^{\text{full}}$) and when ignoring the real-part of the self-energy ($\Re\Sigma = 0$), which is responsible for flattening the Fermi surface.

V. DETAILS OF DΓA CALCULATION

In this section, we explain computational details for DΓA results. For further details and the general procedure how to calculate spin (and charge) fluctuations and from these superconductivity in (λ -corrected), we refer the reader to [5, 20].

First, for solving the impurity problem and calculating local vertices, which act as a starting point, we use the continuous-time quantum Monte-Carlo (CT-QMC) on w2dynamics [15] as an impurity solver [except for $U = 9t$ results, which are taken from the previous results [5] using exact diagonalization (ED)]. We have also

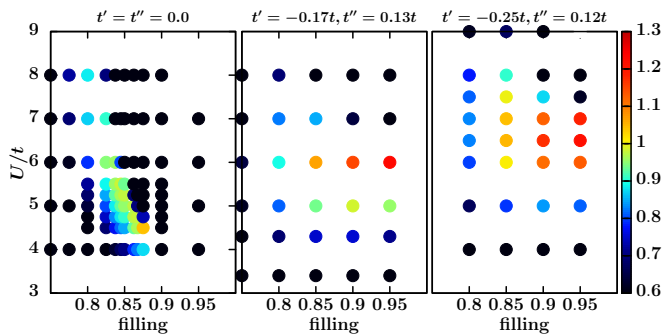


FIG. S.10. Directly calculated points for producing Fig. 3 in the main text. The color corresponds to the superconducting eigenvalue λ at fixed temperature $T = 0.01t$.

checked that both solvers give quantitatively consistent results at $U = 8t, t' = -0.25, t'' = 0.12$.

In the DGA calculations, we separate the Matsubara frequency range into two parts following the previous works [5, 20]. We use 120 (80) Matsubara grids for the case $\beta t = 100, U \geq 5t$ (others) for which the vertices are treated directly. For an extended grid of 2048 Matsubara frequencies on the positive side we use the bare- U contribution instead of the local vertex. This is sufficient to obtain well-converged results even at low temperatures [21]. For momentum grids, we take a 120×120 momentum mesh, which may not be enough to get quantitatively converged results in the critically fluctuating regime (dark magenta region in Fig.3), but elsewhere is sufficient [22]. Nevertheless, this mesh is enough to study the superconductivity dominating region, which is the main scope of this paper.

In Fig. S.10, we display the actually calculated data points. From these points, we obtain the contour plots of Fig. 3 in the main text. For the $t' = t'' = 0$ case, we linearly interpolated some irrelevant (i.e., $\lambda \leq 0.6$) points: $(U/t, n) = (4.75, 0.775), (5.25, 0.775), (5.5, 0.75), (5.5, 0.775), (5.5, 0.8675)$ before making the contour plot.

As for the T_c calculation, we calculate the superconducting λ down to $T = t/100$, and extrapolated the λ vs. T curve (using the form $\lambda \approx a - b \ln(T)$) as in previous publications [5, 20]. As examples, we show in Fig. S.11 DGA results, fit function, and T_c for (a) $U = 7.5t, t' = -0.22t, t'' = 0.14t$ and (b) $U = 6t, t' = -0.24t, t'' = 0.16t$ results (corresponding the $\text{RbSr}_2\text{PdO}_3$ and $A'_2\text{PdO}_2\text{Cl}_2$, respectively).

Besides the superconducting eigenvalue, we also calculate the antiferromagnetic (AFM) susceptibility $\chi_{\text{sp}}(Q_{\text{max}}, \omega = 0)$. DGA respects constraints of the two-dimensionality (i.e., Mermin-Wagner theorem [23, 24]) and does not exhibit an antiferromagnetically ordered phase at finite temperatures (χ_{sp} remains finite). On the other hand, we can naturally expect that AFM will stabilize for a strongly fluctuating regime (dark red region

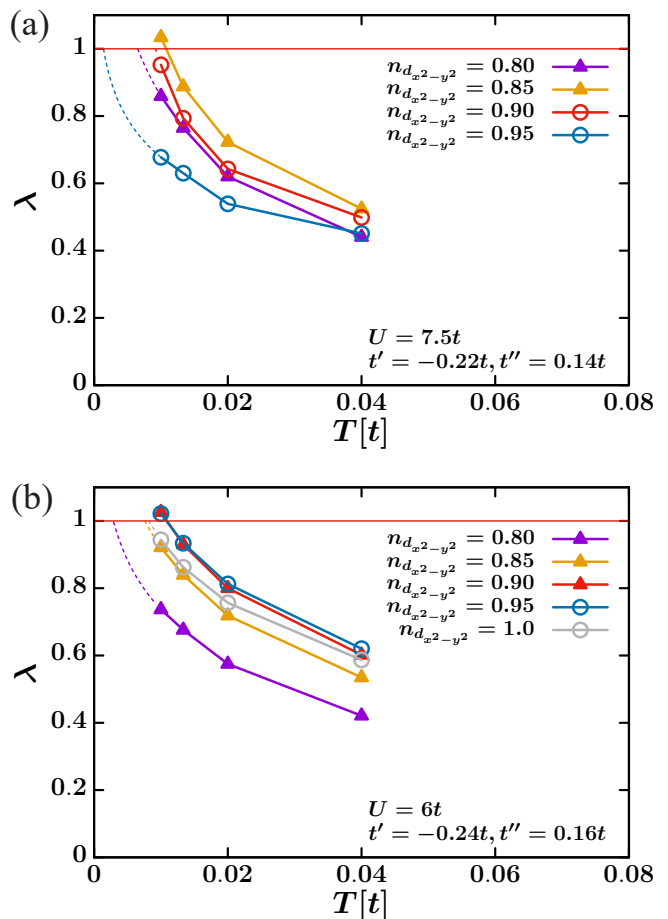


FIG. S.11. Temperature dependence of the superconductivity eigenvalue λ for (a) $U = 7.5t, t' = -0.22t, t'' = 0.14t$ and (b) $U = 6t, t' = -0.24t, t'' = 0.16t$. The extrapolation to $\lambda = 1$ yields T_c .

in Fig. 3 of the main text) once allowing for a weak three-dimensionality, that are present in the actual materials.

VI. WANNIER PROJECTIONS AND CONSISTENCY BETWEEN DFT AND WANNIER BANDS.

Essential for interfacing DFT and DMFT is the Wannier projections. It not only provides the electron hopping parameters for the construction of the minimal low-energy model, but also allows to investigate the degree of localization of the orbitals. An indication for the quality of Wannier projection is its consistency with the target DFT bands. As in previous theoretical studies in the case of nickelates [5, 25], we performed projections for both the single $d_{x^2-y^2}$ band, as well as, all Pd-4d orbitals. In the latter case also additional orbitals that are in the vicinity of, or overlapping with, the Pd bands are included. The single-band $d_{x^2-y^2}$ projection is here used to construct the single-band Hamiltonian for the subse-

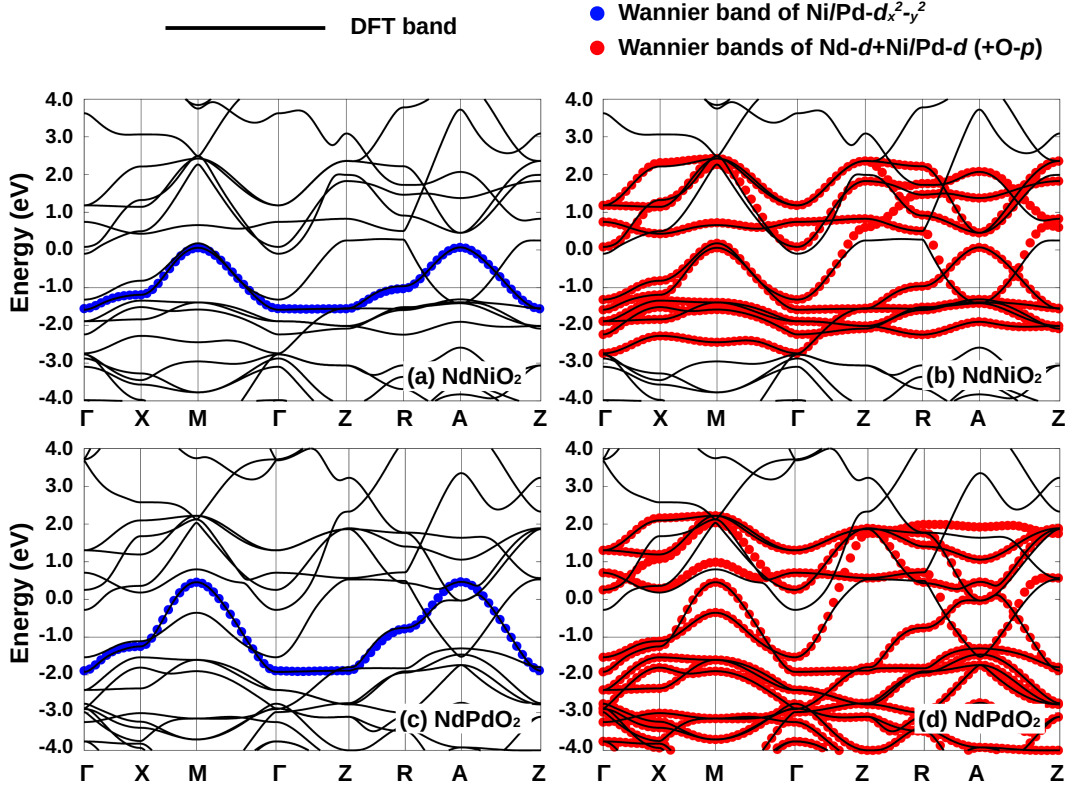


FIG. S.12. DFT band structure of (a,b) NdNiO_2 and (c,d) NdPdO_2 . The blue and red dots represent the Wannier bands of projections onto only the $\text{Pd-}d_{x^2-y^2}$ orbital and the full $\text{Pd-}4d$ plus $\text{Nd } 5d$ orbitals, respectively. In the Wannier projection for NdPdO_2 in (d), further the $\text{O-}p$ orbitals are included in the projection because of the stronger $\text{Pd-}d - \text{O-}p$ hybridization, compared with that of NdNiO_2 .

quent DGA calculation, while the multi-orbital ones are used for DFT+DMFT.

The corresponding hopping parameters of the single-orbital projection and the comparison with the original DFT bands is shown in Fig. S.12(a,c), Fig. S.13(a,c) and Table S.III. All these single-band projections for the $\text{Ni-}d_{x^2-y^2}$ and the $\text{Pd-}d_{x^2-y^2}$ orbital exhibit excellent agreement between the DFT and Wannier band, indicating the quality of these projections and reliability of the corresponding parameters.

For obtaining orbital occupation and spectra, including the positions of pockets, we have done multi-band DMFT calculations, based on the multi-band projections. For the previous calculations of NdNiO_2 , a $\text{Nd(La)-}d + \text{Ni-}d$ basis with 10-bands was adopted. [26] For NdPdO_2 , a projection onto 16 bands, $\text{Nd(La)-}d + \text{Ni-}d + \text{O-}p$, was necessary because of the stronger $\text{Pd-}d - \text{O-}p$ hybridization than in NdNiO_2 , see Fig. S.12(b,d). For $\text{A}'_2\text{PdO}_2\text{Cl}_2$ and $\text{RbSr}_2\text{PdO}_3$, on the other hand, a projection onto only the $\text{Pd-}d$ 5 bands is sufficient, because the other occupied bands are well separated from these $\text{Pd-}d$ bands, see Fig. S.13(b,d). All Wannier bands reproduce the DFT bands well, especially the low energy parts near Fermi

energy.

VII. COMPUTATIONAL DETAILS OF THE VIRTUAL CRYSTAL APPROXIMATION FOR $\text{A}'_2\text{PdO}_2\text{Cl}_2$

The virtual crystal approximation (VCA) [6] has been implemented in the VASP code and applied to the study of $\text{Sn}_x\text{Ge}_{1-x}$ alloys [27]. Such application of VCA in VASP is justified because both VCA and VASP are based on (Vanderbilt) pseudopotentials. However, because WIEN2K uses the full-potential augmented plane-wave and local-orbitals basis set to solve the Kohn-Sham equations, this full VCA is not applicable in WIEN2K. An alternative way to realize atomic substitution and charge doping effect in WIEN2K is to modify the core and valence electron states in the input configuration files [28].

We perform VCA calculations for $\text{A}'_2\text{PdO}_2\text{Cl}_2$ using WIEN2K and VASP as outlined in the last paragraph. The corresponding bands are shown in Fig. S.14(a) and (b), respectively. As the comparison shows, both codes give exactly the same bands, especially the parts below

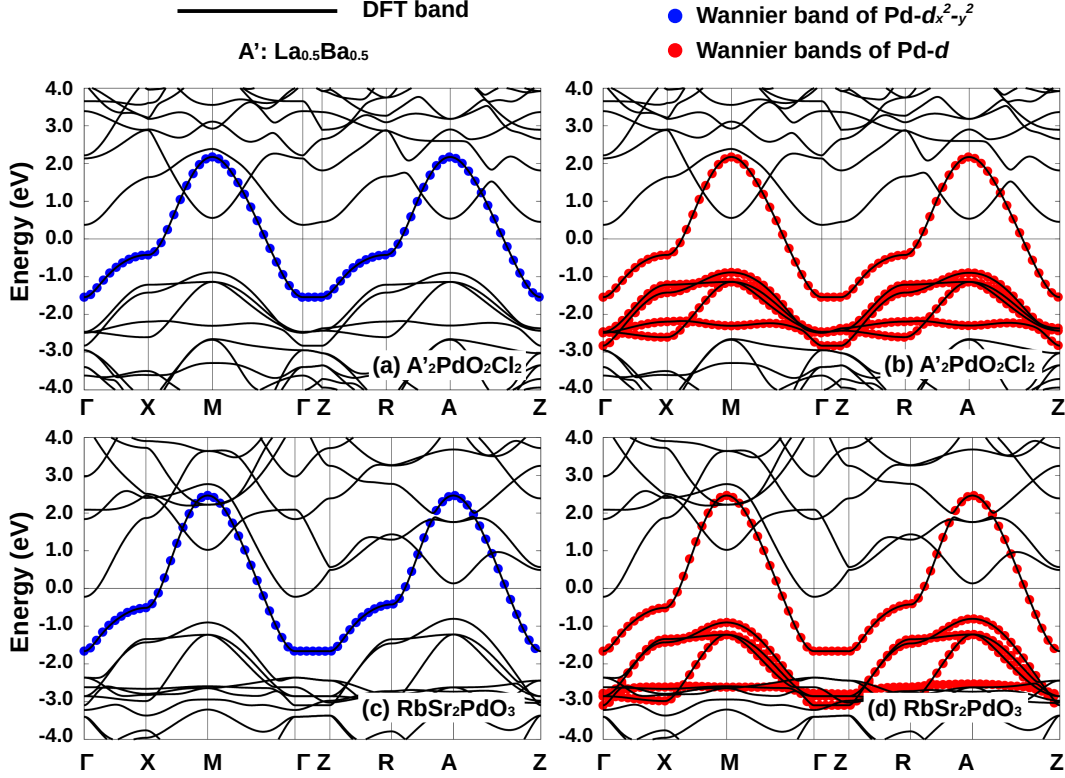


FIG. S.13. DFT band structure of (a,b) $A'_2\text{PdO}_2\text{Cl}_2$ and (c,d) $\text{RbSr}_2\text{PdO}_3$. The blue and red dots represent the Wannier bands of the projection onto (a,c) only the $\text{Pd-}d_{x^2-y^2}$ and (b,d) onto all $\text{Pd-}4d$ bands, respectively.

~ 2.0 eV.

In Fig. S.14(a), we additionally show the Wannier band of the $\text{Pd } d_{x^2-y^2}$ orbital. The excellent agreement between DFT and Wannier band indicates the high quality of our Wannier projection and localization of the $\text{Pd-}d_{x^2-y^2}$ orbital. In Fig. S.14(c,d), we compute and show the DFT band of (c) undoped $\text{Ba}_2\text{PdO}_2\text{Cl}_2$ and (d) $\text{La}_2\text{PdO}_2\text{Cl}_2$. In the former and later cases the bivalent Ba^{2+} and trivalent La^{3+} lead to nominal Pd^{2+} ($4d^8$) and Pd^0 ($4d^{10}$), respectively. Please note that in $\text{La}_2\text{PdO}_2\text{Cl}_2$ due to the hybridization between $\text{La-}d$ and $\text{Pd-}d$, the oxidation state of Pd is in fact between Pd^{1+} and Pd^0 , as in $A'_2\text{PdO}_2\text{Cl}_2$.

In Fig. S.14(c,d), we show again the $\text{Pd-}d_{x^2-y^2}$ Wannier band taken from Fig. S.14(a), and add (subtract) a constant, leading to the red dots in Fig. S.14(c,d). The shifted Wannier bands exhibit excellent consistency between the $\text{Pd-}d_{x^2-y^2}$ bands in Fig. S.14(c,d), indicating the atomic substitution and charge doping effects can, in fact, be well described by a rigid band shift. This explains why the simplified VCA method in WIEN2K yields essentially the same results as VASP.

VIII. PHONON CALCULATIONS AND STRUCTURAL DISTORTIONS OF LaPdO_2

To investigate the dynamical stability of NdPdO_2 , we compute its phonon spectra with the frozen phonon method (finite displacement method) using the PHONONY [29] code interfaced with VASP [30, 31]. For the phonon spectra of the other two palladates, $A'_2\text{PdO}_2\text{Cl}_2$ and $\text{RbSr}_2\text{Pd}_2\text{O}_3$, similar calculations can be found in Fig. 11(b,c) of Ref. [3]. Here, to increase computational efficiency and to avoid the issue of bad convergence arising from $\text{Nd-}4f$ bands, we replace Nd by La . Previous theoretical research [32] and the experimental confirmation of superconductivity in both Ca-doped LaNiO_2 [33] and Sr-doped NdNiO_2 [34, 35] indicate that the replacement of Nd by La does not significantly change the physics. T_c is reduced a bit in the La compound, which likely originates mainly from different levels of disorder. The corresponding phonon spectra of the ideal $P4/mmm$ phase of LaPdO_2 is shown in Fig. S.15 and the structural evolution is shown in Fig. S.16(a-c).

We first check the phonon spectra of the ideal $P4/mmm$ phase LaPdO_2 . Using the PBESol functional, the optimized lattice parameters are $a=b=4.126$ Å, $c=3.265$ Å. Compared with $\text{La}(\text{Nd})\text{NiO}_2$, the a (c) lattice

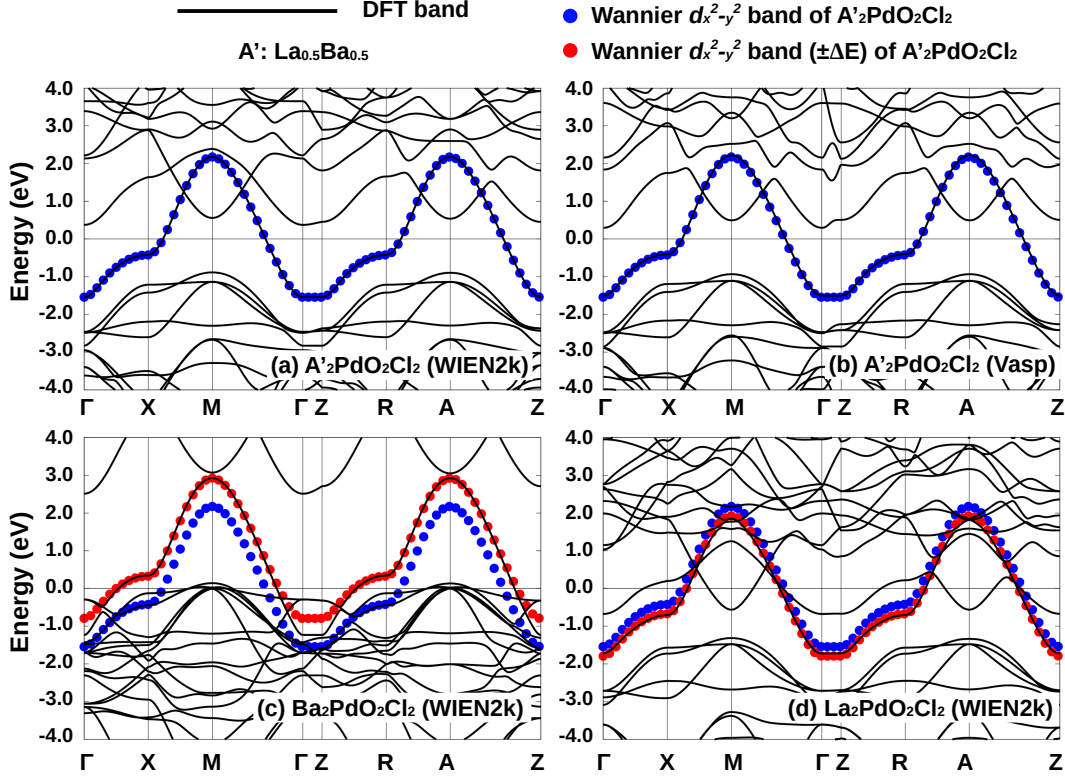


FIG. S.14. DFT band structure of $A'^2\text{PdO}_2\text{Cl}_2$ ($A'=\text{La}_{0.5}\text{Ba}_{0.5}$) in the virtual crystal approximation comparing (a) WIEN2K (simplified version, see text) and (b) VASP. The blue dots are the Wannier band for the Pd- $d_{x^2-y^2}$ orbital as calculated by the WIEN2K Wannier projection. (c) and (d) DFT band structure of $\text{Ba}_2\text{PdO}_2\text{Cl}_2$ and $\text{La}_2\text{PdO}_2\text{Cl}_2$, respectively, as calculated in WIEN2K. The Wannier band of the Pd- $d_{x^2-y^2}$ orbital in (a) is also shown (blue dots). The red dots are a constant energy shift of these by (c) $+0.75$ eV and (d) -0.25 eV.

parameter is increased (reduced) by 6.1% (2.1%). The instability of $P4/mmm$ LaPdO_2 is evidenced by negative frequencies in its phonon spectra [Fig. S.15(a,b)]. The phonon spectra and atomic-resolved DOS are computed by employing a $2\times 2\times 2$ supercell of LaPdO_2 , which is shown in Fig. S.16(a). As shown in Fig. S.15, the phonon spectrum of $P4/mmm$ LaPdO_2 reveals a dynamical instability at both the X [$q=(1/2,0,0)$] and A [$q=1/2,1/2,1/2$] points of the q -path. These unstable phonons are in fact consistent with those in SmNiO_2 , YNiO_2 [36], LuNiO_2 [37, 38], and EuNiO_2 [38]. We further predict the structures with lower symmetry and total energies on the basis of the eigenvectors (atomic vibrations) induced by the X_2^- , A_3^+ mode and the combination between both of them, using group theory and the workflow of [37]. The eigenvector of the unstable phonon at X -point is X_2^- [37] and is related to a ferroelectric distortion perpendicular to the PdO_2 layers. The phonon mode at the A -point is A_3^+ and is related to the in-plane rotation of PdO_4 planers, leading to a $I4/mcm$ symmetry [38] [Fig. S.16(b)] phase. Further, the combination of X_2^- and A_3^+ corresponds to an orthorhombic distortion, i.e.,

the $Pbcn$ phase [Fig. S.16(c)]. After (non-spin-polarized) DFT-PBESol structural relaxations, the $I4/mcm$ and $Pbcn$ phase are energetically more stable than the ideal $P4/mmm$ phase by 102 meV and 225 meV per LaPdO_2 formula unit, respectively. We hence conclude that the $P4/mmm$ ($Pbcn$) structures are corresponding to high (low) temperature phases.

We additionally compute the Pd- $d_{x^2-y^2}$ hopping of the ideal $P4/mmm$, tetragonal $I4/mcm$ and the low symmetry $Pbcn$ phase of LaPdO_2 . As shown in Table S.III, the 1st nearest hopping t is reduced from -537 meV in ideal $P4/mmm$ phase to -357 meV in $I4/mcm$ phase, finally to -304 meV in $Pbcn$ phase. Due to the both, the reduced t and t' , the DFT bandwidth is reduced from ~ 4.4 eV in the $P4/mmm$ phase to ~ 2.4 eV in the $Pbcn$ phase. The t in $I4/mcm$ and $Pbcn$ phase is even smaller than that in NdNiO_2 (-397 meV), indicating stronger correlations than in the ideal $P4/mmm$ phase.

For the comparison between DFT and Wannier bands of distorted $Pbcn$ phase of LaPdO_2 , see Fig. S.17. Compared with the bands of ideal $P4/mmm$ phase, the bandwidth of $Pbcn$ phase of LaPdO_2 is effectively reduced

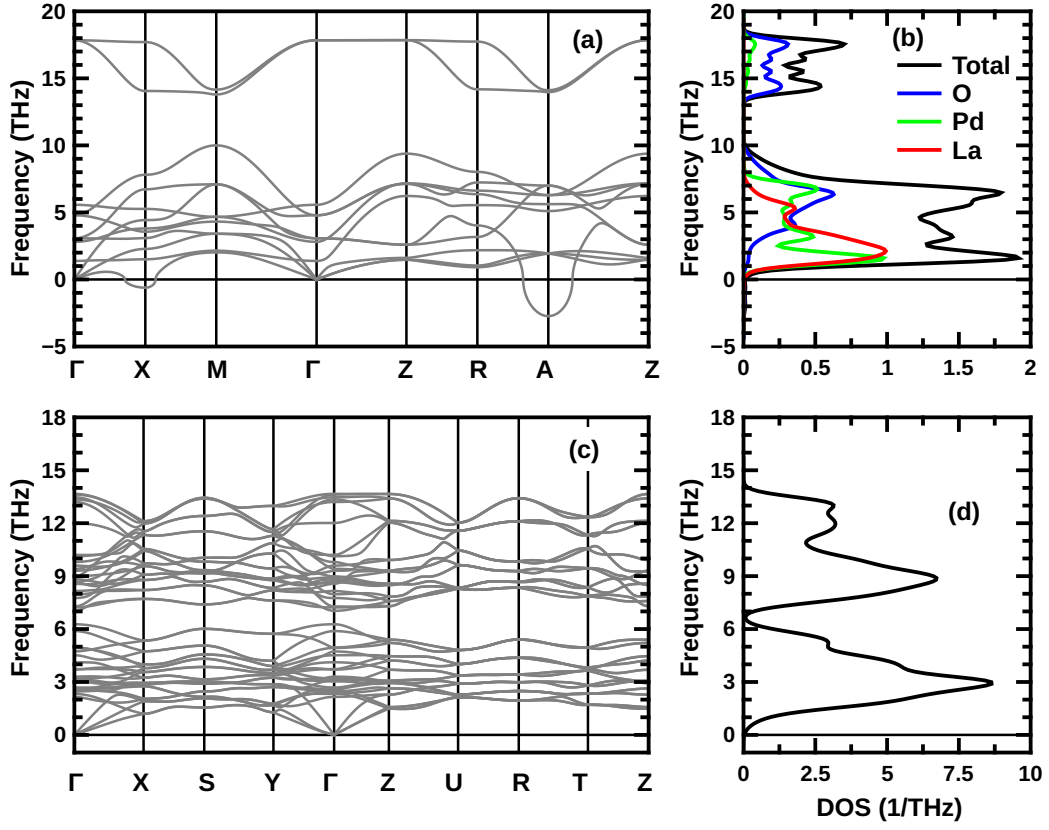


FIG. S.15. (a,c) DFT phonon spectra and (b,d) phonon density of states of the (fully relaxed) ideal *P4/mmm* (a,b) and distorted *Pbcn* (c,d) phase of LaPdO₂.

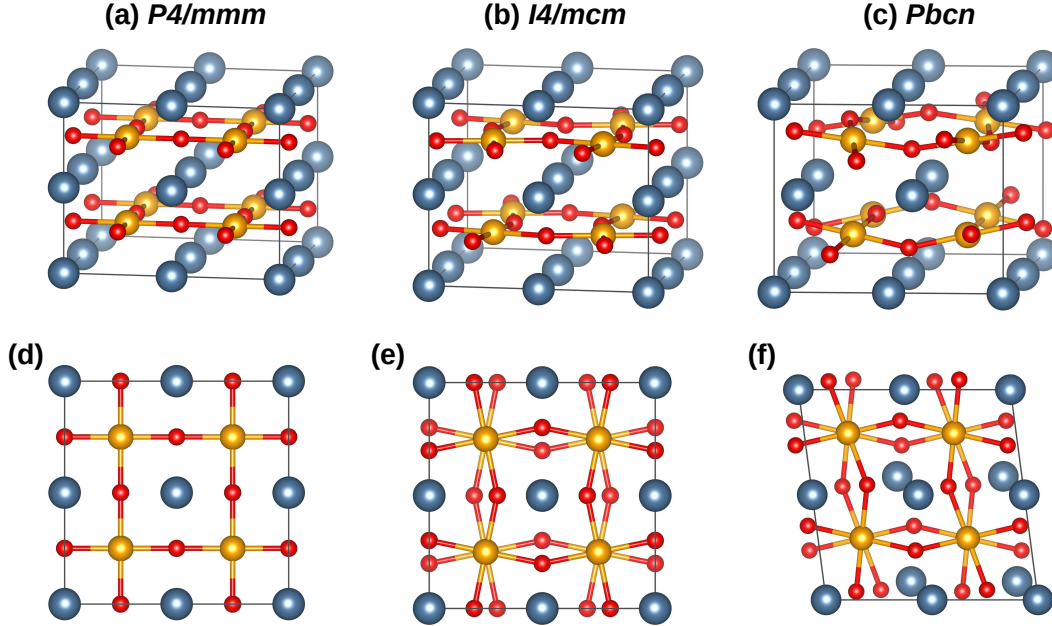


FIG. S.16. DFT-relaxed structures of LaPdO₂: (a,d) ideal tetragonal *P4/mmm* phase; (b,e) tetragonal *I4/mcm* phase; (c,f) orthorhombic *Pbcn* phase. The panels (d,e,f) are the top-view along the *z*-direction (001) of panels (a,b,c), respectively.

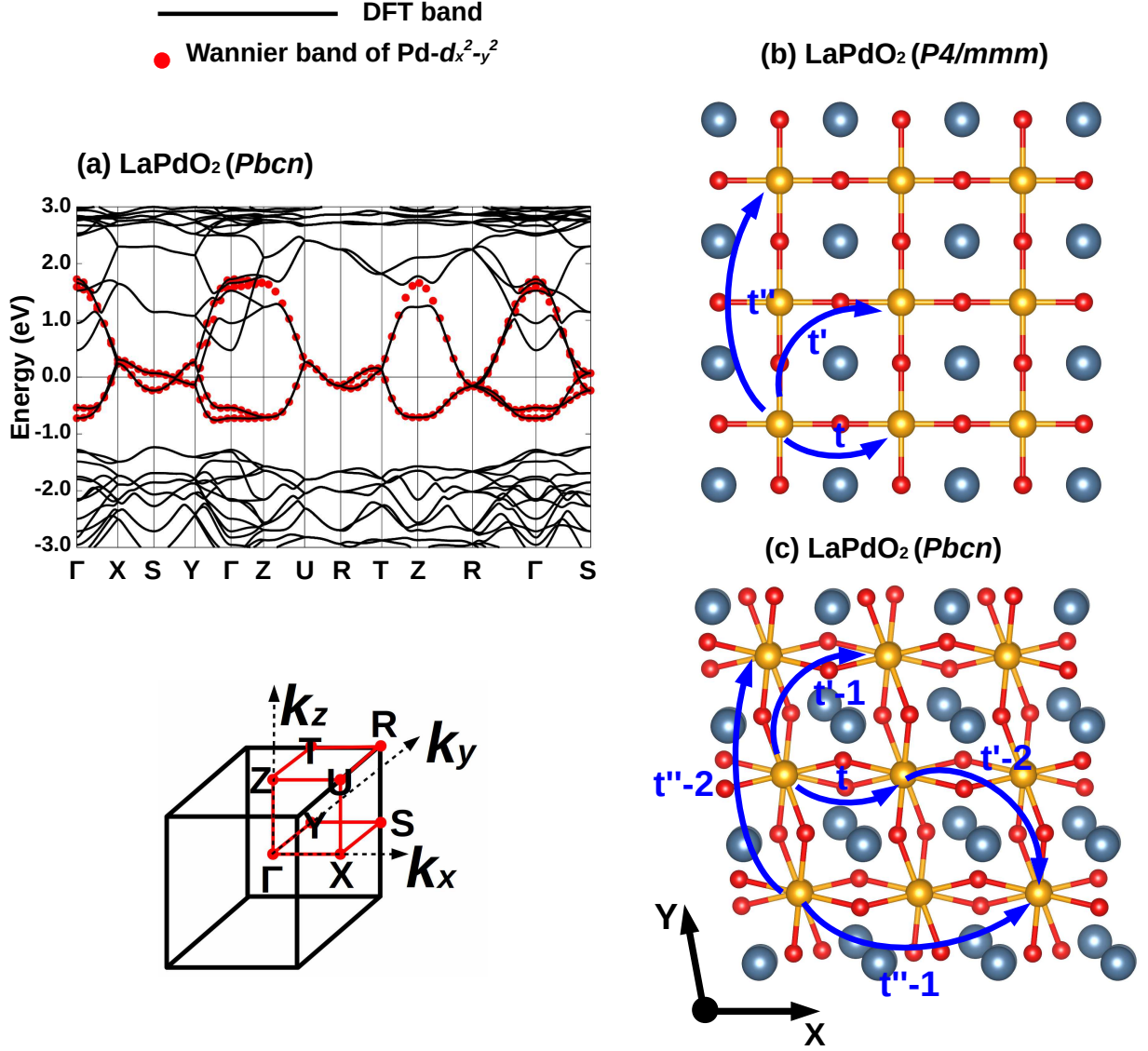


FIG. S.17. (a) Comparison between DFT and Wannier tight-binding Hamiltonian bands of distorted $Pbcn$ phase of LaPdO_2 , the bottom-left panel shows the Brillouin zone. Major hopping terms of (b) ideal $P4/mmm$ and (c) distorted $Pbcn$ phase of LaPdO_2 . The t , t' and t'' indicates the 1st, 2nd and 3rd nearest hopping between $\text{Pd-}d_{x^2-y^2}$ orbital, obtained from Wannier projection calculations. Please note that in the distorted $Pbcn$ phase of LaPdO_2 , both the t' and t'' are anisotropic due to the orthorhombic distortion, i.e., the hoppings along (110) and $(\bar{1}\bar{1}0)$, as well as along the (200) and (020) direction, respectively. The $t'-1$ (-2) and $t''-1$ (-2) corresponds to the 1st (2nd) row value of $Pbcn$ phase in Table S.III.

from 4.60 eV in $P4/mmm$ phase to 2.45 eV in $Pbcn$ phase, these are consistent with the reduced major hoppings shown in Table S.III. Additionally, in both Table S.III and Fig. S.17(b,c) we demonstrate the emergence of anisotropic hoppings terms of t' and t'' along (110) and $(\bar{1}\bar{1}0)$, as well as along the (200) and (020) direction, respectively. Such anisotropic hopping is a consequence of the orthorhombic distortion in $Pbcn$ phase.

IX. DFT+ U MAGNETIC TOTAL ENERGIES OF $A_2\text{PdO}_2\text{Cl}_2$

To investigate the magnetic ground state of $A_2\text{PdO}_2\text{Cl}_2$ ($A=\text{La}_{0.5}\text{Ba}_{0.5}$), we perform DFT+ U ($U=3$ eV, 3.3 eV and 4 eV) calculations with a $\sqrt{2}\times\sqrt{2}\times 1$ supercell, as shown in Fig. S.18(a). In each layer of $(\text{PdO}_2)_2$, there are two Pd sites, and in total two such $(\text{PdO}_2)_2$ layers in the supercell. We define the following three types of magnetic order: FM (inter-layer FM and intra-layer FM), A-AFM (inter-layer AFM and

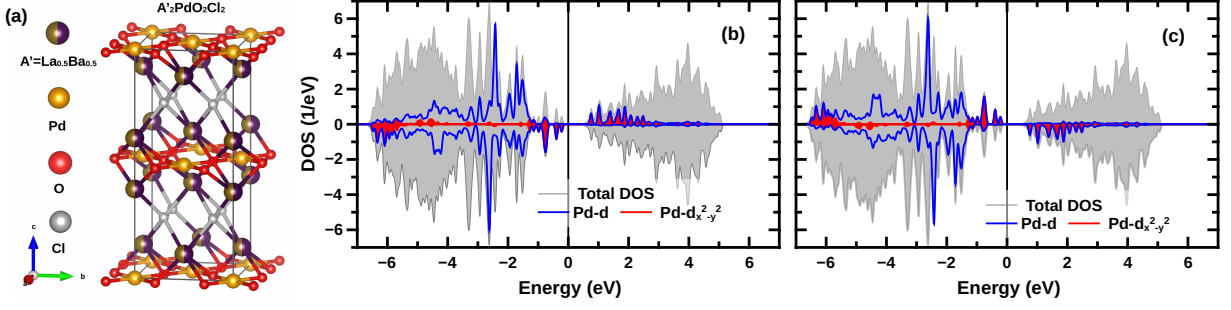


FIG. S.18. (a) DFT crystal structure of $A_2PdO_2Cl_2$ and (b,c) density-of-states of antiferromagnetic DFT+ U at $U=3.3$ eV for the two inequivalent Pd sites of the supercell of (a) and G -type antiferromagnetism. The upper and lower panels of (b,c) denote the spin-up and -down channels respectively.

TABLE S.III. Wannier hoppings of the Pd $d_{x^2-y^2}$ orbital for the ideal $P4/mmm$, tetragonal $I4/mcm$ and orthorhombic $Pbcn$ phase of $LaPdO_2$ (in unit of meV). The t , t' and t'' indicate the 1st, 2nd and 3rd nearest hopping along the real-space vectors of (100), (110) and (200), respectively. The ratios between t'/t and t''/t are also given. The emergence of the second $Pbcn$ values is due to the orthorhombic distortion in $Pbcn$ phase, leading to nonequivalent t' and t'' along (110) and $(\bar{1}10)$ as well as between the (200) and (020) direction.

Phase	t	t'	t''	t'/t	t''/t
$P4/mmm$	-537	97	-71	-0.181	0.131
$I4/mcm$	-357	77	-15	-0.214	0.043
$Pbcn$	-304	56	3	-0.184	0.014
	-304	95	-4	-0.313	-0.012

intra-layer FM), G -AFM (inter-layer AFM and intra-layer AFM) [39]. Our DFT+ U calculations confirm G -AFM to be the magnetic ground state for all U values. Specifically, the G -AFM order is for the aforementioned three U values, more stable than FM order by 84 meV, 103 meV and 162 meV per $A_2PdO_2Cl_2$ chemical formula. The magnetic moments in FM state for all three considered U values are $\sim 0.2 \mu_B$, $0.25 \mu_B$ and $0.40 \mu_B$ per Pd, such small moments are not very effective in reducing their total energy. As a consequence, the total energy of FM states are only < 1 meV ($U = 3$ eV), ~ 2 meV ($U = 3.3$ eV) and ~ 2 meV ($U = 4$ eV) lower than those of PM states (per $A_2PdO_2Cl_2$ chemical formula). We find the energies obtained from A -AFM setup calculations are the same as for PM order because they converge to PM state, indicating the inter-layer (anti-ferromagnetic) couplings/interactions between PdO_2 layers are negligible and too weak to stabilize A -AFM order. This can be explained by the long distance between PdO_2 layers along the z -direction ($\sim 7.32 \text{ \AA}$ according to DFT-PBESol structural relaxations).

Fig. S.18(b,c) show the density-of-states (DOS) of G -type antiferromagnetic order in $A_2PdO_2Cl_2$, resolved for the two inequivalent sites and spin-up and spin-down

channel ($U=3.3$ eV as in our multi-orbital DMFT calculations). With such a degree of correlations a gap of ~ 0.6 eV is opened in the presence of G -AFM order. The highest occupied orbital is Pd- $d_{x^2-y^2}$, indicating a single-band AFM orders that is similar to cuprates. The magnetic moment projected onto the Pd site is $0.55 \mu_B$ ($U=3$ eV), $0.57 \mu_B$ ($U=3.3$ eV) and $0.63 \mu_B$ ($U=4$ eV) per Pd, residual magnetic moments are located at the O- p orbital and interstitially. This demonstrates the d - p hybridization between Pd and O is stronger than that in nickelates. This puts palladates in-between cuprates and nickelates, as already indicated from the energy levels in Fig. 1 of the main text.

- [1] J. P. Perdew, A. Ruzsinszky, G. I. Csonka, O. A. Vydrov, G. E. Scuseria, L. A. Constantin, X. Zhou, and K. Burke, *Phys. Rev. Lett.* **100**, 136406 (2008).
- [2] J. P. Perdew, K. Burke, and M. Ernzerhof, *Phys. Rev. Lett.* **77**, 3865 (1996).
- [3] M. Hirayama, T. Tadano, Y. Nomura, and R. Arita, *Phys. Rev. B* **101**, 075107 (2020).
- [4] K. Lee, B. Y. Wang, M. Osada, B. H. Goodge, T. C. Wang, Y. Lee, S. Harvey, W. J. Kim, Y. Yu, C. Murthy, S. Raghun, L. F. Kourkoutis, and H. Y. Hwang, *arXiv:2203.02580* (2022).
- [5] M. Kitatani, L. Si, O. Janson, R. Arita, Z. Zhong, and K. Held, *npj Quantum Materials* **5**, 59 (2020).
- [6] L. Bellaiche and D. Vanderbilt, *Phys. Rev. B* **61**, 7877 (2000).
- [7] F. Tran and P. Blaha, *Phys. Rev. Lett.* **102**, 226401 (2009).
- [8] G. H. Wannier, *Phys. Rev.* **52**, 191 (1937).
- [9] N. Marzari and D. Vanderbilt, *Phys. Rev. B* **56**, 12847 (1997).
- [10] I. Souza, N. Marzari, and D. Vanderbilt, *Phys. Rev. B* **65**, 035109 (2001).
- [11] N. Marzari, A. A. Mostofi, J. R. Yates, I. Souza, and D. Vanderbilt, *Rev. Mod. Phys.* **84**, 1419 (2012).
- [12] A. A. Mostofi, J. R. Yates, Y.-S. Lee, I. Souza, D. Vanderbilt, and N. Marzari, *Computer physics communications* **178**, 685 (2008).

- [13] J. Kuneš, R. Arita, P. Wissgott, A. Toschi, H. Ikeda, and K. Held, *Computer Physics Communications* **181**, 1888 (2010).
- [14] V. I. Anisimov, I. V. Solovyev, M. A. Korotin, M. T. Czyżyk, and G. A. Sawatzky, *Phys. Rev. B* **48**, 16929 (1993).
- [15] M. Wallerberger, A. Hausoel, P. Gunacker, A. Kowalski, N. Parragh, F. Goth, K. Held, and G. Sangiovanni, *Computer Physics Communications* **235**, 388 (2019).
- [16] E. Gull, A. J. Millis, A. I. Lichtenstein, A. N. Rubtsov, M. Troyer, and P. Werner, *Rev. Mod. Phys.* **83**, 349 (2011).
- [17] J. Kaufmann and K. Held, [arXiv:2105.11211](https://arxiv.org/abs/2105.11211) (2021).
- [18] J. E. Gubernatis, M. Jarrell, R. N. Silver, and D. S. Sivia, *Phys. Rev. B* **44**, 6011 (1991).
- [19] A. W. Sandvik, *Phys. Rev. B* **57**, 10287 (1998).
- [20] M. Kitatani, R. Arita, T. Schäfer, and K. Held, *Journal of Physics: Materials* **5**, 034005 (2022).
- [21] M. Kitatani, T. Schäfer, H. Aoki, and K. Held, *Phys. Rev. B* **99**, 041115 (2019).
- [22] T. Schäfer, A. A. Katanin, M. Kitatani, A. Toschi, and K. Held, *Phys. Rev. Lett.* **122**, 227201 (2019).
- [23] P. C. Hohenberg, *Phys. Rev.* **158**, 383 (1967).
- [24] N. D. Mermin and H. Wagner, *Phys. Rev. Lett.* **17**, 1133 (1966).
- [25] J. Karp, A. S. Botana, M. R. Norman, H. Park, M. Zingl, and A. Millis, *Phys. Rev. X* **10**, 021061 (2020).
- [26] Other multi-band projections, use Nd interstitial-*s* instead of Nd *5d* [40]. This interstitial-*s* orbital is formed by a complex hybridization between Nd-*f*, Nd-*d* and Nd(La)-*d* orbital, or Ni-*d*+pocket-bands [41, 42].
- [27] C. Eckhardt, K. Hummer, and G. Kresse, *Phys. Rev. B* **89**, 165201 (2014).
- [28] <https://www.mail-archive.com/wien@zeus.theochem.tuwien.ac.at/msg11726.html>.
- [29] A. Togo and I. Tanaka, *Scripta Materialia* **108**, 1 (2015).
- [30] G. Kresse and J. Furthmüller, *Computational materials science* **6**, 15 (1996).
- [31] G. Kresse and J. Furthmüller, *Phys. Rev. B* **54**, 11169 (1996).
- [32] A. S. Botana and M. R. Norman, *Phys. Rev. X* **10**, 011024 (2020).
- [33] S. Zeng, C. Li, L. E. Chow, Y. Cao, Z. Zhang, C. S. Tang, X. Yin, Z. S. Lim, J. Hu, P. Yang, and A. Ariando, *Science Advances* **8**, eabl9927 (2022).
- [34] S. Zeng, C. S. Tang, X. Yin, C. Li, M. Li, Z. Huang, J. Hu, W. Liu, G. J. Omar, H. Jani, Z. S. Lim, K. Han, D. Wan, P. Yang, S. J. Pennycook, A. T. S. Wee, and A. Ariando, *Phys. Rev. Lett.* **125**, 147003 (2020).
- [35] D. Li, B. Y. Wang, K. Lee, S. P. Harvey, M. Osada, B. H. Goodge, L. F. Kourkoutis, and H. Y. Hwang, *Phys. Rev. Lett.* **125**, 027001 (2020).
- [36] F. Bernardini, A. Bosin, and A. Cano, *Phys. Rev. Materials* **6**, 044807 (2022).
- [37] A. Subedi, [arXiv preprint arXiv:2203.11922](https://arxiv.org/abs/2203.11922) (2022).
- [38] C. Xia, J. Wu, Y. Chen, and H. Chen, *Phys. Rev. B* **105**, 115134 (2022).
- [39] Due to the shift between the 1st and 2nd (PdO₂)₂ layers, the Pd of the next layer is in-between the two Pd sites of the previous layer in A₂PdO₂Cl₂. Hence, C-type AFM order (inter-layer FM and intra-layer AFM) is not possible in A₂PdO₂Cl₂.
- [40] Y. Nomura, M. Hirayama, T. Tadano, Y. Yoshimoto, K. Nakamura, and R. Arita, *Phys. Rev. B* **100**, 205138 (2019).
- [41] F. Lechermann, *Phys. Rev. B* **101**, 081110 (2020).
- [42] F. Lechermann, *Phys. Rev. X* **10**, 041002 (2020).